

# Radio Science

## RESEARCH ARTICLE

10.1029/2019RS006936

### Key Points:

- We carried out a HF ray tracing simulation for three proposed equatorial SuperDARN-type radars for the African equatorial sector
- We used realistic ionospheres deduced from the IRI and geomagnetic field geometries from the IGRF to simulate SuperDARN radar backscatter
- We analyzed the performances predicted for these radars, and following this analysis provide recommendations for their future development

### Correspondence to:

C. M. Michael,  
cmm41@le.ac.uk  
chizurumok@gmail.com

### Citation:

Michael, C. M., Yeoman, T. K., Wright, D. M., Milan, S. E., & James, M. K. (2020). A ray tracing simulation of HF ionospheric radar performance at African equatorial latitudes. *Radio Science*, 55, e2019RS006936. <https://doi.org/10.1029/2019RS006936>

Received 30 JUL 2019

Accepted 13 JAN 2020

Accepted article online 21 JAN 2020

## A Ray Tracing Simulation of HF Ionospheric Radar Performance at African Equatorial Latitudes

**Chizurumoke M. Michael<sup>1,2</sup> , Tim K. Yeoman<sup>1</sup> , Darren M. Wright<sup>1</sup>, Steve E. Milan<sup>1</sup> , and Matthew K. James<sup>1</sup> **

<sup>1</sup> Radio and Space Plasma Physics Group, Department of Physics and Astronomy, University of Leicester, Leicester, UK,  
<sup>2</sup> Department of Physics and Electronics, Federal University, Otuoke, Yenagoa, Bayelsa State, Nigeria

**Abstract** High-frequency (HF) coherent radars are widely applied for studying electrodynamic processes in the Earth's upper atmosphere and ionosphere. Super Dual Auroral Radar Network (SuperDARN) is an international network of such radars located at high- and middle-latitude regions in the Northern and Southern Hemispheres. A major criterion of the HF coherent radar technique entails that the HF waves propagate orthogonal to the geomagnetic field lines (aspect angle  $\leq 1^\circ$ ) in the ionospheric irregularity region from where backscatter originates. In this paper we present an HF ray tracing simulation of the performance of three proposed equatorial HF radar systems for the African equatorial sector. We use a number of realistic average ionospheres deduced from the International Reference Ionosphere (IRI) 2012 model and magnetic field geometries from the International Geomagnetic Reference Field (IGRF) to determine likely propagation paths and orthogonality conditions for such radar systems. The east-west azimuth ( $\sim 25^\circ$  range) has a significant likelihood of achieving a SuperDARN-type backscatter in the African equatorial sector, mainly due to the prevailing magnetic field geometry. This analysis provides a feasibility study for developing a SuperDARN-like radar for studying the equatorial ionosphere over the African longitude sector, for example, in determining the technical radar characteristics such as preferable operating frequencies, antenna boresight orientation, and azimuth coverage and provides a simulation of the expected localization of radar backscatter as a function of radar location and beam direction, as well as the time of day, season, and sunspot number.

### 1. Introduction

The high-frequency (HF) coherent radars have in recent years become a dominant instrument for studying the formation, evolution, and convection of magnetic field-aligned ionospheric electron density irregularities. The irregularities drift at the  $E \times B$  velocity in the *F* region ionosphere making it possible to measure the ionospheric plasma convection from the motion of irregularities in this region. Operating the radar at this frequency band, typically between 8 and 14 MHz, allows the radio waves to become sufficiently refracted by the ionosphere such that their wave vectors are oriented orthogonal to geomagnetic field lines, which are near-vertical at high latitude (Greenwald et al., 2017). Consequently, coherent backscatter from the transmitted signals due to the field-aligned decameter-scale ionospheric plasma irregularities are generated (e.g., Chisham et al., 2007). Such backscatter due to plasma density irregularities at *E* and *F* regions is commonly known as ionospheric scatter.

A multitude of scientific results and understanding of the characteristics and structure of the terrestrial plasma environment have been achieved through organized ground-based HF radar techniques, such as the Super Dual Auroral Radar Network (SuperDARN) (Chisham et al., 2007; Greenwald et al., 1995; Nishitani et al., 2019). The SuperDARN radars, apart from observing ionospheric scatter, also see backscatter from the ground, known as ground scatter, and from other sources such as meteor trail echoes and the sea (Ribeiro et al., 2011). Such ground scatter is due to rays reflecting from the ionosphere back to the Earth's surface. The capability of distinguishing ionospheric scatter from such ground scatter in existing SuperDARN data remains a work in progress. For example, Ribeiro et al. (2011) described an improved technique for identifying ground scatter and ionospheric scatter in midlatitude SuperDARN data. Such research is outside the scope of the present study. Likewise, a major difficulty encountered prior to SuperDARN and other ground-based radars used for studying ionospheric plasma irregularities was the determination of the ray-paths of HF waves, which are strongly influenced by the ionosphere (Villain et al., 1984). This difficulty

meant that it was hard to precisely interpret the geolocation of the backscattered signals. In this regard, significant successes have been accomplished in rectifying and enhancing the geolocation accuracy of HF radar backscatter through application of ray tracing modeling of HF propagation through realistic ionospheres using modeled and measured data and combinations of the two (e.g., André et al., 1997; Chisham et al., 2008; Yeoman et al., 2001, 2008). However, a completely accurate way of determining backscatter geolocation is yet to be achieved.

The SuperDARN project was originally initiated to study the high-latitude ionosphere (Chisham et al., 2007; Greenwald et al., 1995), which implies that many existing studies on HF radar applications for ionospheric research are concentrated on the high latitudes, and more recently the midlatitudes (Nishitani et al., 2019). However, there were a few studies over the African ionospheric latitude sector using coherent HF zenithal radar (e.g., Blanc & Houngninou, 1998; Blanc et al., 1996; Farges et al., 1999) and oblique HF radar (e.g., Hanuise & Crochet, 1978) techniques for measuring and studying electron density irregularities. These early studies focused mainly on studying the electrodynamics of the equatorial electrojet (EEJ) using HF radar experiments conducted in Africa (e.g., Hanuise & Crochet, 1977, 1979, 1981a, 1981b). It is important to emphasize here that HF radar measurements have been successfully applied in studying other terrestrial magnetosphere-ionosphere physical processes (Chisham et al., 2007). Many of these attempts at studying the ionosphere over the African equatorial latitude region using HF radar systems were largely short-lived scientific campaigns such as the International Equatorial Electrojet Year between 1993 and 1994. The implication of this is that the ensuing analyses in these studies may be limited in providing a broader understanding of, for example, the long-term structure and evolution of the irregularities.

Recently, Lawal et al. (2018) made a proposition for using SuperDARN-like HF radar techniques in studying the African low-latitude equatorial ionosphere. They suggested that establishing such a scientific project will lead to enhanced understanding of complex electrodynamics and physical processes such as the EEJ, predominant in this region, which are yet to be fully understood. The societal benefits from the enhanced scientific understanding, which such a project would provide are ever increasing in today's world. For example, critical infrastructure like power grids and Global Navigation Satellite System are impacted on by the space weather processes partly resulting from the near-Earth terrestrial plasma dynamics.

Interestingly, the SuperDARN topographical outlook has been expanding in recent times, covering more of the midlatitude ionosphere and moving toward the low-latitude ionosphere (Greenwald et al., 2017; Nishitani et al., 2019; Ribeiro et al., 2012). Extending it to the equatorial region, especially the African latitude sector that has remained virtually unstudied using a SuperDARN-like technique, will expand its usability and lead to an all-encompassing global ionospheric plasma convection map, studying related magnetospheric and ionospheric phenomena and enhanced understanding of the electrodynamics predominant in the equatorial ionosphere.

The SuperDARN radars rely on the perpendicularity of magnetic field-aligned irregularities with the HF radar wave vectors to provide measurements. Determining the possible spatial distribution where the orthogonality requirement of the SuperDARN radar technique can be achieved is a major step toward the realization of the scientific objectives espoused in Lawal et al. (2018). A ray tracing simulation can be applied in determining bespoke SuperDARN-like radar operating requirements over equatorial latitudes and also for a broader understanding of the behavior of HF electromagnetic wave propagation through a realistic equatorial ionosphere. Such ray tracing programs have been extensively applied for determining the probable locations that orthogonality between the HF radar wave vector and the geomagnetic field that can be realized under various ionospheric conditions at high latitude (e.g., Villain et al., 1984) and midlatitude (e.g., Nishitani & Ogawa, 2005). For example, prior to the development of Hokkaido SuperDARN radar at a midlatitude location (Nishitani et al., 2019), a ray tracing simulation similar to the present study was performed in order to identify possible ionospheric backscatter areas at midlatitude (Nishitani & Ogawa, 2005). This study showed that the distributions of possible areas of achieving ionospheric backscatter differ depending on the local time and geomagnetic activity. Given that the terrestrial magnetic field geometry varies enormously in latitude, the existing high-latitude analysis cannot predict system performance at the equatorial latitudes.

In this study, we present an HF ray tracing simulation using a modified version of the algorithm developed by Jones and Stephenson (1975) using realistic equatorial ionospheric parameters deduced from the

International Reference Ionosphere (IRI) 2012 model. This analysis is devoted more on characterizing possible areas of ionospheric backscatter for typical SuperDARN radars at African equatorial latitude. However, a section of the study provides a brief analysis of possible locations of ground scatter for such equatorial region. In addition, this analysis will provide a feasibility study for developing a SuperDARN-like radar for studying the equatorial ionosphere over the African latitude sector. For example, in determining technical radar characteristics such as preferable operating frequency and antenna boresight azimuths with optimal chances of achieving SuperDARN-type backscatter over the region. Here, section 2 describes the ray tracing procedure and the ionospheric models employed. It also covers in detail the method adopted for this study. Section 3 presents the results from the study, including a detailed analysis of the occurrence, elevation angle, and localization of simulated radar backscatter as a function of the radar beam azimuth. Subsequently, the implications of the results and ensuing design recommendations are discussed in section 4.

Many HF ray tracing studies involve examining observed measurements by existing HF radars with ray tracing modeling. Unfortunately, there are no currently existing SuperDARN-like radars at the locations selected for the present analysis. As such, the interpretations of results in this paper will be compared with previous related studies, many of which are for the high- and middle-latitude ionosphere. Also, the results presented here represent average expected radar performance under a variety of ionospheric conditions. Only a limited set of ionospheric conditions have been studied here; thus, the observations provided here will be subjected to further validation when SuperDARN-like radar measurements over this region become available.

## 2. Ray Tracing Simulation

In order to predict the spatial region and combinations of radar operating parameters, such as frequency, with backscattering potential for a SuperDARN-like radar in the equatorial latitude, we have performed ray tracing simulations using representative ionospheric electron density profiles inferred from the IRI model.

### 2.1. Ionospheric Models

The ionospheric electron density profiles used in this study have been deduced from the IRI 2012 model using the NeQuick option for the topside electron density (e.g., Bilitza et al., 2014). The ionosphere is a continuously changing region of the terrestrial atmosphere due to photoionization and recombination mainly dictated by extreme ultraviolet rays from the Sun. As such, carrying out ray tracing modeling for this continuously varying region can best be done by producing an averaged profile that encapsulates the ionospheric electron density at the geographic location being studied.

A similar ray tracing simulation by de Larquier et al. (2011) based on the IRI ionospheric electron density profile for a midlatitude ionosphere has shown good correlation for ground scatter during a geomagnetically quiet period. However, correlating radar measurements of ionospheric scatter with ray tracing are more problematic given that a typical ray tracing model assumes uniform distribution of ionospheric irregularities. As such, it only predicts possible scatter distributions but cannot account for the presence or absence of the irregularities essential to observe ionospheric scatter (de Larquier et al., 2013). Nonetheless, de Larquier et al. (2013) demonstrated that for a midlatitude ionosphere the intrinsic uncertainties in the IRI model have insignificant effect on the modeled ionospheric backscatter. The IRI is an empirical model, as such it performs better at midlatitude with a large available database than, for example, the African equatorial latitude sector with a relatively sparse database (Bilitza et al., 2014). However, previous ionospheric studies have shown that the IRI 2012 model data for the equatorial ionosphere of the African longitude sector have a good correlation with measured data. For example, Tariku (2015) showed that the IRI-2012 model with the NeQuick topside option was generally good in estimating the total electron content derived from GPS measurements.

A double alpha-Chapman model has been fitted with the IRI model for different diurnal, seasonal, and solar cycle periods in order to create broadly representative ionospheric conditions. The analysis (not shown here) did not indicate any clear dissimilarity at the three locations used for this study (see Table 1 and Figure 1). On the other hand, the  $F_2$  layer critical frequencies are higher during solar maximum year (2014) than the solar minimum year (2009) and during the local afternoon than at the local midnight and morning. These variations are nothing new as they are primarily controlled by ionization and recombination of electrons. Considering that seasonal variability and the variability at the three simulated radar locations are not significant, the ionospheric profiles shown in Table 2, representing the general trends of peaks and troughs were

**Table 1**  
*Simulated Radar Locations*

Country	Place	Geographic coordinate	Label
Sierra Leone	Njala University	7.93°N, 11.76°W	Bo Njala radar
Nigeria	University of Port Harcourt	4.89°N, 6.92°E	Port Harcourt radar
Ethiopia	Bahir Dar University	11.55°N, 37.36°E	Bahir Dar radar

selected and used in the present study regardless of the geographic location differences of the simulated radars. The ionospheric profiles shown in the Table 2, include critical frequency of *F* layer (*f<sub>oF2</sub>*), height of maximum of *F* layer (*hmF2*), scale height of *F* layer (*hF2*), critical frequency of *E* layer (*f<sub>oE</sub>*), height of maximum of *E* layer (*hmE*), and scale height of *E* layer (*hE*) parameters for varying diurnal and solar activity periods. In our ray tracing analysis, these ionospheric profiles represent a horizontally uniform ionosphere and there is no magnetic field. They are designated as ionospheric profile (A-H) in the subsequent analysis and discussions.

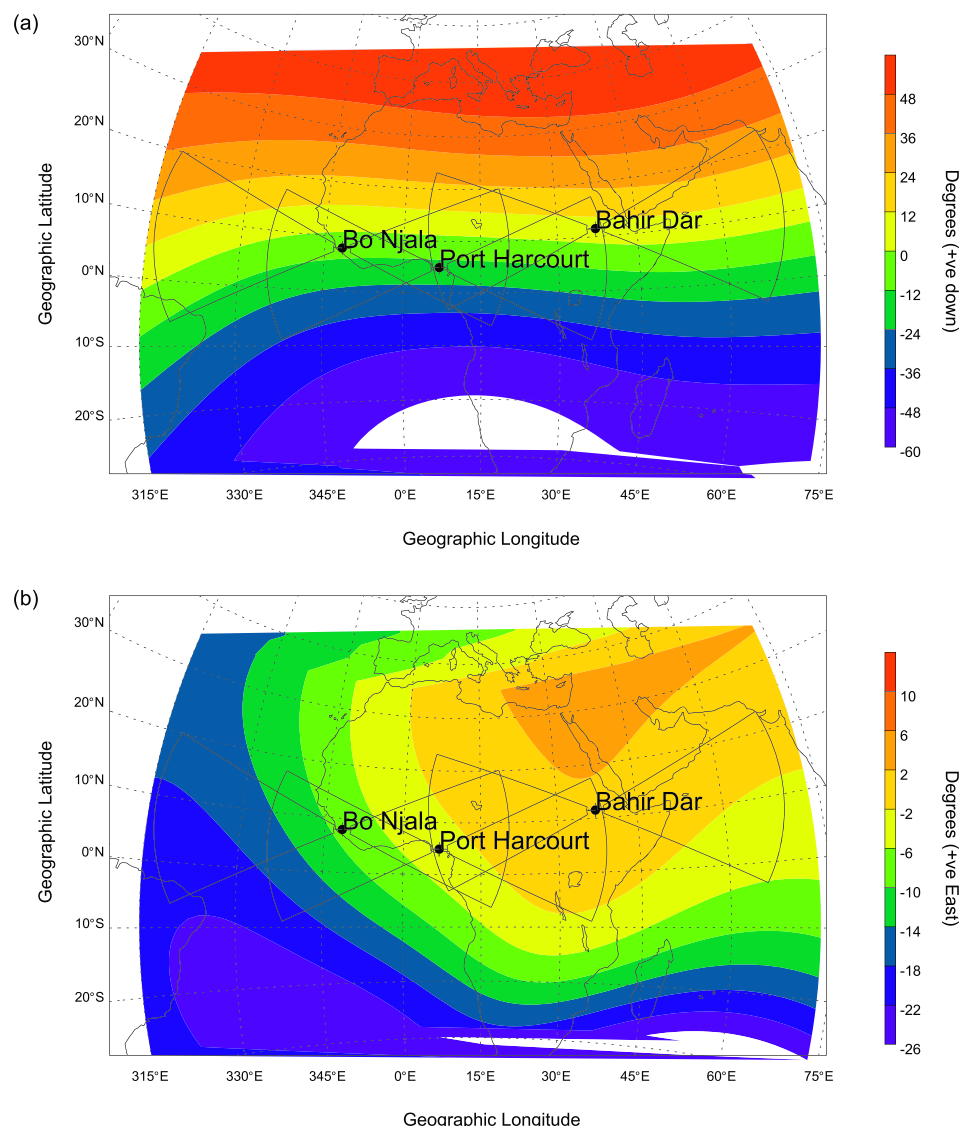


**Figure 1.** Map showing the Earth's magnetic (a) inclination (I) and (b) declination (D) over the locations and fields of view (FOVs) of the simulated radars. Each side of the FOV ranges 3,000 km from the radar location. The Earth's magnetic field is derived from IGRF model (Thébault et al., 2015).

**Table 2**  
*Characteristics of Ionospheric Density Profiles*

Profile	Interval/solar activity	F region (Chapman layer)	E region (Chapman layer)
A	0 LT-minimum	$f_{oF2} = 3.9$ MHz, $hmF2 = 291$ km, $hF2 = 56$ km	$f_{oE} = 0.49$ MHz, $hmE = 110$ km, $hE = 10$ km
B	6 LT-minimum	$f_{oF2} = 5.7$ MHz, $hmF2 = 290$ km, $hF2 = 60$ km	$f_{oE} = 2.68$ MHz, $hmE = 110$ km, $hE = 10$ km
C	12 LT-minimum	$f_{oF2} = 8.2$ MHz, $hmF2 = 320$ km, $hF2 = 55$ km	$f_{oE} = 2.77$ MHz, $hmE = 110$ km, $hE = 10$ km
D	18 LT-minimum	$f_{oF2} = 6.7$ MHz, $hmF2 = 308$ km, $hF2 = 57$ km	$f_{oE} = 1.45$ MHz, $hmE = 110$ km, $hE = 10$ km
E	0 LT-maximum	$f_{oF2} = 7.0$ MHz, $hmF2 = 358$ km, $hF2 = 57$ km	$f_{oE} = 0.55$ MHz, $hmE = 110$ km, $hE = 10$ km
F	6 LT-maximum	$f_{oF2} = 8.6$ MHz, $hmF2 = 360$ km, $hF2 = 60$ km	$f_{oE} = 3.30$ MHz, $hmE = 110$ km, $hE = 10$ km
G	12 LT-maximum	$f_{oF2} = 10.8$ MHz, $hmF2 = 388$ km, $hF2 = 53$ km	$f_{oE} = 3.20$ MHz, $hmE = 110$ km, $hE = 10$ km
H	18 LT-maximum	$f_{oF2} = 9.0$ MHz, $hmF2 = 376$ km, $hF2 = 50$ km	$f_{oE} = 1.30$ MHz, $hmE = 110$ km, $hE = 10$ km

The simulated radar locations (Table 1) are selected to provide a broad coverage of the equatorial ionosphere over the African longitude sector. Also, we consider locations such as university campuses as feasible locations for siting a SuperDARN-style radar in Africa.

## 2.2. Description of Methods

This study employed the three-dimensional (3-D) ray tracing model developed by Jones and Stephenson (1975).

Realistic ionospheric electron densities profiles inferred from the IRI-2012 model (e.g., Bilitza et al., 2014) and the latest International Geomagnetic Reference Field (IGRF-12) (Thébault et al., 2015) are coupled with the ray tracing model. In this case, the IRI is used to calculate the refractive index using the noncollisional transverse Appleton-Hartree formula as a function of electron density and frequency (Davies, 1990). The refraction that a ray encounters as it propagates through the ionosphere is a determining factor of the locations where the ray has the potential of achieving orthogonality with the Earth's magnetic field. The orthogonality angle,  $\alpha = \text{mod}(90^\circ - \Omega)$ , where  $\Omega$  is the angle between the HF wave vector  $\mathbf{k}$  and the magnetic field vectors  $\mathbf{B}$ . This, in the case of HF SuperDARN radars, represents the region where backscatter from electron density irregularities maybe observed as illustrated in Figure 2. The values of  $\alpha$ , with the criterion being that  $\alpha \leq 1^\circ$ , are used to predict the spatial distribution of potential regions where backscatter can be achieved and such scattering regions are further analyzed based on predicted elevation angle, altitude, and ground range.

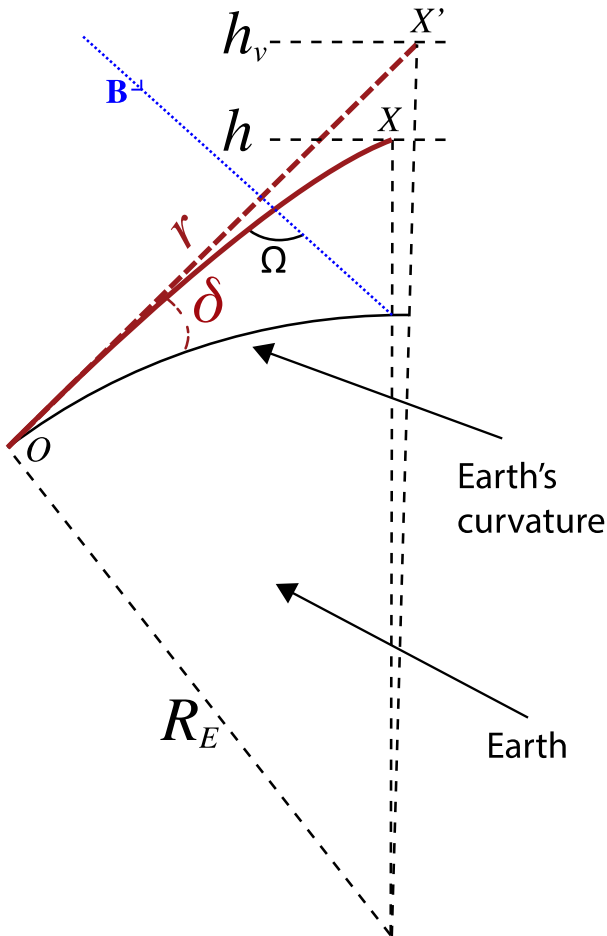


**Figure 2.** Schematic diagram illustrating ray propagation path traversing the ionosphere. The solid curve is a realistic path, and the dashed line is the line-of-sight path,  $h$  and  $h_v$  represent the physical and virtual altitudes, respectively. The angle between HF wave vector  $\mathbf{k}$  and vector of geomagnetic field  $\mathbf{B}$  is  $\Omega$ , such that the orthogonality angle,  $\alpha = \text{mod}(90^\circ - \Omega)$ , while  $\delta$  is the elevation angle,  $r$  is the slant range along the propagation path,  $R_E$  is the radius of the Earth, and  $\mathbf{B}$  is the geomagnetic field (After:de Larquier et al., 2013).

We employed eight different ionospheric models (A–H) as presented in Table 2. These profiles include the  $E$  and  $F_2$  Chapman layers with associated scale heights ( $hF2$  and  $hE$ ). The derived critical plasma frequency is between 3.9 and 10.8 MHz for the  $F_2$  region ( $f_{oF2}$ ) and between 0.5 and 3.3 MHz for the  $E$  region ( $f_{oE}$ ). For each of the ionospheric profiles, we performed ray tracings using multiple transmit frequencies (12, 16, 20, and 24 MHz) and elevation angles between  $1^\circ$  and  $90^\circ$  in steps of  $0.1^\circ$ . Although existing SuperDARN radars mainly operate from 8 to 20 MHz, here, we have selected 12, 16, 20, and 24 MHz transmit frequencies because they represent a set of uniform workable frequencies for all the ionospheric conditions used in this study. For example, a ray tracing simulation using 8 MHz as shown in Figure 3 (top panel), reasonably achieved orthogonality for Profile A, which is a weak ionosphere with a low  $f_{oF2}$ . In Figure 3 (middle panel) for Ionospheric Profile D with medium  $f_{oF2}$ , there is a possibility of ionospheric scatter with good orthogonality but it can be seen that it is collocated with densely spaced one, two, and three hop ground scatter from  $\sim 500$ –2,000 km ground range, and it is likely that the ground scatter will be more powerful (Milan et al., 1997) and dominate the measurements, preventing the collection of

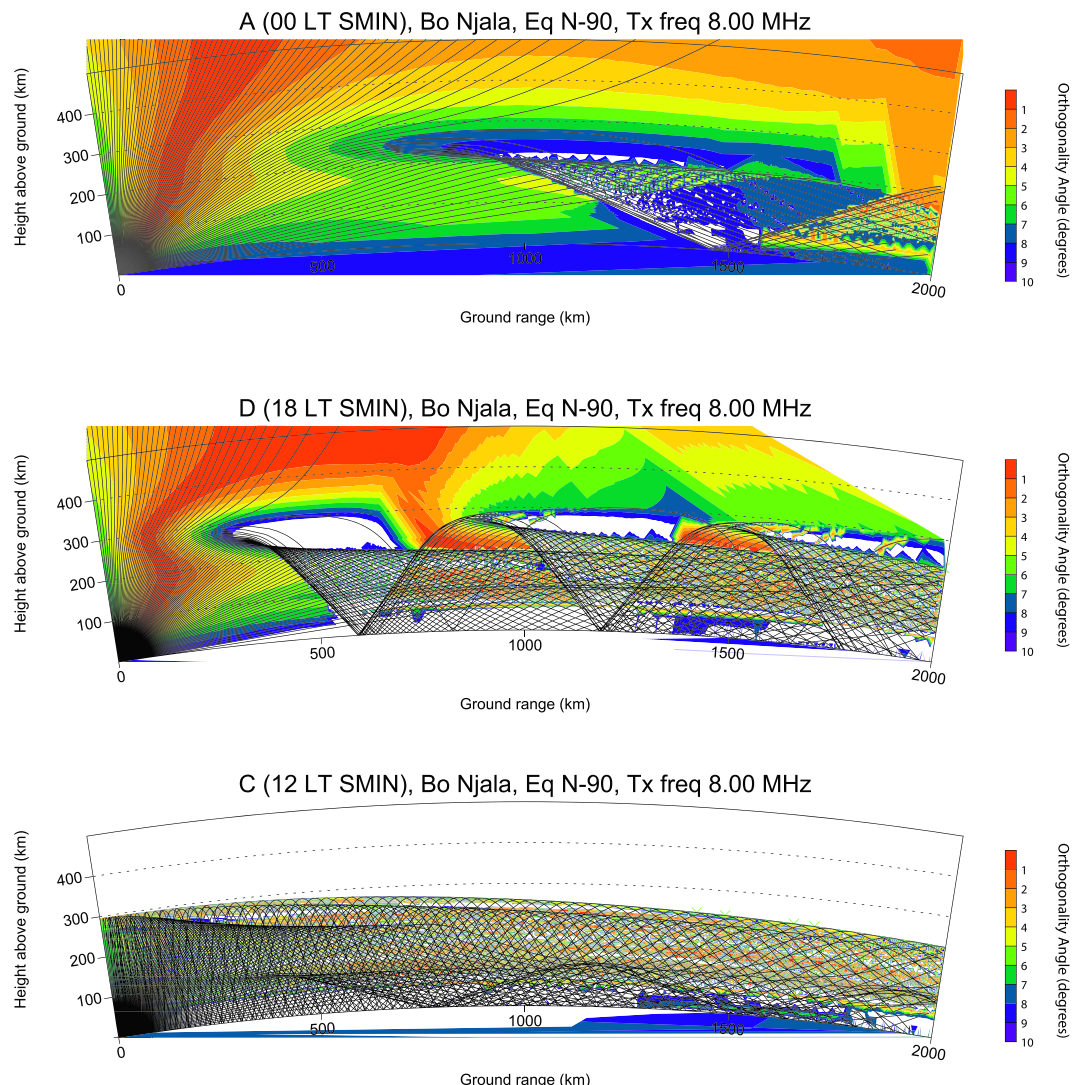


**Figure 3.** Ray tracing for simulated HF radars at Bo Njala location from an azimuth of  $90^\circ$  measured from North geographic coordinate at 8 MHz frequency and with elevation angle rays from  $0^\circ$  to  $90^\circ$ . The color codes represent perpendicularity  $\leq 10^\circ$  between wave vector and the geomagnetic field. Plot derived using the Ionospheric Profiles A, D, and C parameters as shown in the top, middle, and bottom panels, respectively.

useful ionospheric scatter. In the event that the ionospheric critical frequency exceeds the radar transmit frequency, multiple reflections occur, and the radar field of view (FOV) is saturated with ground scatter, making the detection of ionospheric backscatter unlikely. This is illustrated in Figure 3 (bottom panel) for Ionospheric Profile C (at noon with medium  $f_{oF2}$ ) where a lot of reflections occur when the critical frequency of ionosphere is greater than the transmit frequency, which leads to a significant occurrence of ground scatter due to multiple hop propagation. Such profiles with medium and high  $f_{oF2}$  are more typical of the profiles (see Table 2) employed in this study as deduced from the IRI model. It is not unexpected given that  $f_{oF2}$  is usually large at equatorial latitude. A single antenna array cannot cover 8–24 MHz with an acceptable beam pattern, as a result, a frequency range of 12–24 MHz is optimal for the equatorial region, rather than 8–20 MHz typical of higher-latitude SuperDARN radars and this frequency range is explored here.

Furthermore, collisions are ignored in the simulation since they mainly result in wave absorption. As such, transmitted rays follow trajectories influenced primarily by the gradients of the ionospheric electron density. This influence of the ionosphere is greater on the horizontally inclined rays than the vertically inclined rays. The orthogonality between the ray vector and the Earth's magnetic field is then deduced from the IGRF model. Given that the SuperDARN radars produce backscatter where the wave vector and geomagnetic field

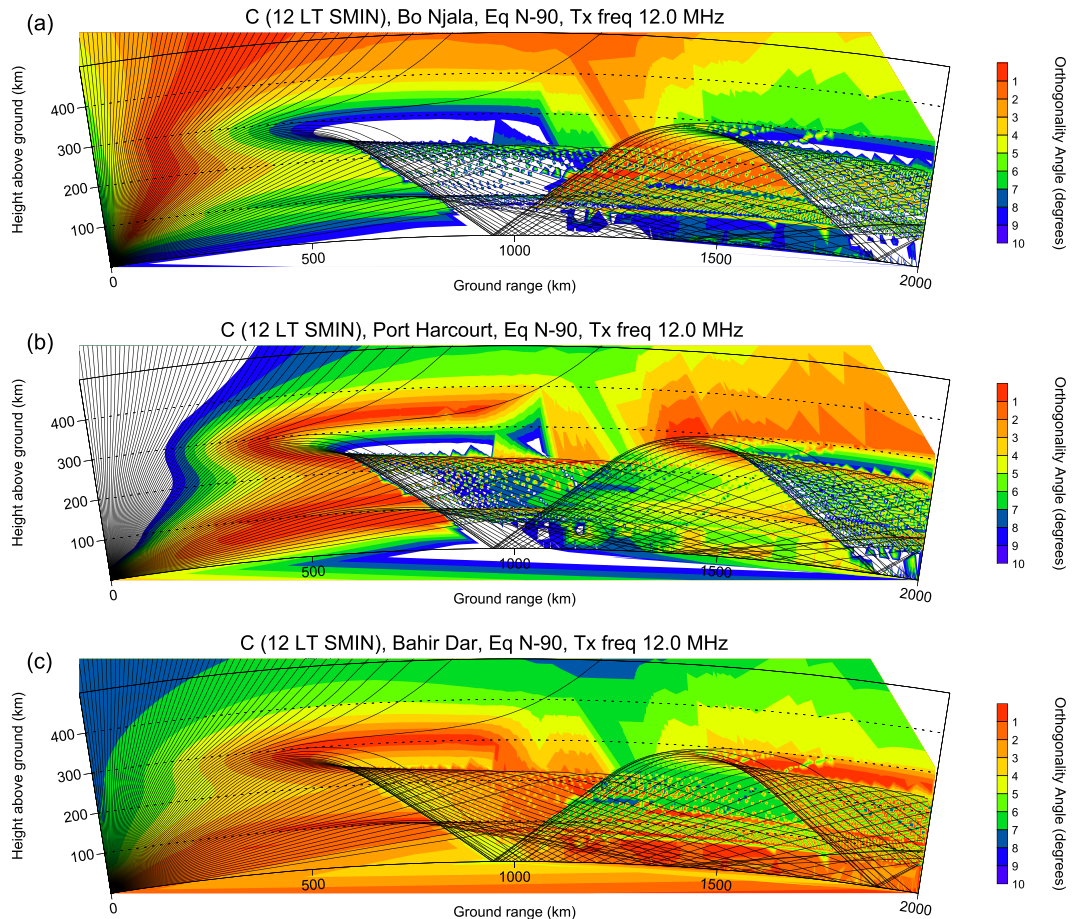


**Figure 4.** Ray tracing for simulated HF radars at Bo Njala (a), Port Harcourt (b), and Bahir Dar (c) locations, from an azimuth of  $90^\circ$  measured from North geographic coordinate at 12 MHz frequency and with elevation angle rays from  $0^\circ$  to  $90^\circ$ . The color codes represent perpendicularity  $\leq 10^\circ$  between wave vector and the geomagnetic field. Plot derived using the Ionospheric Profile C parameters.

are orthogonal, the points on the simulated ray trajectory where  $\alpha \leq 1^\circ$  are selected with accompanying latitude, longitude, altitude, group path, elevation angle, and ground range parameters. The regions that meet these criteria are commonly referred to as simulated radar backscatter or backscatter in the following analysis. In some of the analyses where there is need for spatial visualization, the orthogonality scales are expanded to  $\alpha \leq 10^\circ$  to allow easy illustration of variability but with emphasis placed on where  $\alpha \leq 1^\circ$ . The ray points are binned in group path in steps of 1 km, and the projected angle is calculated using spherical trigonometry with the maximum horizontal range and altitude of raypaths set at 2,500 and 500 km, respectively.

### 3. Analysis

Figure 4 shows the results of ray tracing for one example simulation derived using Profile C at noon with medium  $f_{oF2}$  ionospheric parameters (see Table 2), an azimuth of  $90^\circ$  from geographic North and a 12 MHz transmit frequency and at the three different equatorial locations. Panels (a)–(c) represent Bo Njala, Port Harcourt, and Bahir Dar radars, respectively. The altitude above the ground and ground range both in kilometers are plotted along the y axis and x axis, respectively, while the color coding represents the variation in regions of perpendicularity  $\alpha \leq 10^\circ$  to the Earth's magnetic field across  $1^\circ$  to  $90^\circ$  elevation angles. The orthogonality is calculated for  $0.1^\circ$  steps of elevation angle, while the rays are shown at  $1^\circ$  steps, for clarity.

As shown in Figure 4, at Bo Njala (top panel), there is more backscatter predicted from vertically inclined rays ( $\sim 44\text{--}75^\circ$ ) as indicated in red regions than from lower elevation angles. The regions with orthogonality (deep red) are pronounced at altitudes above 100 km, spreading out at 200 km, the bottom side F region

ionosphere, and above 300 km. At lower elevation angles, orthogonality is achieved up to 2,000 km ground range. Also, a curved region that is depleted of orthogonality ( $\alpha \leq 5^\circ$ ) is apparent at about 350 km ground range and 300 km altitude, spreading out to 1,200 km in range. This depleted region coincides with the *F* region Pedersen rays from waves with elevation angles between  $38^\circ$  and  $41^\circ$ . Features of Pedersen rays, which represent rays that are at the limit between reflection off and penetration into the ionosphere, appear between  $9^\circ$  and  $11^\circ$  for the *E* region. In addition, propagation from lower elevation angles produces patches of backscatter below the *F* region Pedersen rays at ground ranges between 1,200 and 1,800 km. These patches arise due to rays between  $1^\circ$  and  $38^\circ$  reflecting off the ground at one hop  $\approx 950$  km and two hop  $\approx 1,850$  km then radiating back to the ionosphere from where they achieve orthogonality. Therefore, at Bo Njala, regions that meet the orthogonality condition ( $\alpha \leq 1^\circ$ ) vary with the propagation angle. The locations where orthogonality seemed to be achieved at Bo Njala is corroborated by the Earth's magnetic field geometry shown in Figure 1. Here, Bo Njala lies almost under the magnetic equator with a near horizontal magnetic inclination angle of its FOV, while the magnetic declination tilts to the west compared to at high latitude of the same longitude where it is almost  $0^\circ$ . Note here that the orthogonality associated with the near-vertical rays is predominantly due to Earth's magnetic field geometries rather than the influence of the ionospheric electron density gradients.

At Port Harcourt (Figure 4, middle panel), vertically oriented rays above  $45^\circ$  elevation are depleted of backscatter. The lower elevation rays ( $\sim 1\text{--}45^\circ$ ) have more backscatter compared to Bo Njala where vertical rays produced more backscatter than the oblique rays. Regions where orthogonality are achieved can be seen from 50 to 400 km altitude, covering both the *E* and *F* region ionosphere, which is different from Bo Njala, which had little orthogonality below 100 km altitude. Moreover, regions with orthogonality ( $\alpha \leq 1^\circ$ ) appear from ground ranges of  $\approx 250$  km away from the radar to 2,000 km maximum range. These features are slightly different from Bo Njala where propagation from near-vertical rays achieved orthogonality at ground ranges closer to the radar. Also, features of Pedersen rays from elevation angles between  $39^\circ$  and  $41^\circ$  for *F* region and  $9^\circ$  and  $11^\circ$  for *E* region are noticeable but with a smaller curved region depleted of orthogonality ( $\alpha \leq 5^\circ$ ) compared to Bo Njala. Similar to Bo Njala, there are also patches of backscatter from rays reflecting off the ground back to the ionosphere where they achieve orthogonality.

Figure 4 (bottom panel), representing Bahir Dar radar is similar to Port Harcourt radar in terms of structure of regions where orthogonality are achieved apart from having improved orthogonality. There is no curved region depleted of orthogonality ( $\alpha \leq 5^\circ$ ) at Bahir Dar. Both Port Harcourt and Bahir Dar radars, as shown from the Earth's magnetic field geometry (Figure 1), have almost horizontal magnetic inclination, except that Port Harcourt radar is north of the equator, while Bahir Dar is south. Therefore, despite the same ionospheric profile (C at noon with medium *f<sub>oF2</sub>*), propagation azimuth and transmit frequency being used for the ray tracing in Figure 4, it can be seen that radar performance, in terms of where orthogonality with values ( $\alpha \leq 1^\circ$ ) are achieved, varies across the three different locations. The distribution of possible ground and ionospheric scatter at three equatorial locations in Figure 4 is quite typical of high- and mid-latitude SuperDARN radar data (e.g., de Larquier et al., 2013; Milan et al., 1997).

In the preceding analysis, we have demonstrated that the likelihood of achieving orthogonality will vary at the three different geographic locations. In other words, the potential of achieving orthogonality, which in practical terms translates to SuperDARN-type backscatter, will vary not only with radar locations but also with ionospheric electron density gradient, radar propagation azimuth, and operating frequency. The ray tracing simulation in Figure 5 demonstrates the variation in radar performance as a result of different ionospheric conditions (different times of day). Figure 5 is the same azimuth as in Figure 4, but the location, Bo Njala, and 12 MHz transmit frequency are the same across the three panels, indicating from top to bottom, the A, F, and H ionospheric profiles, respectively (see Table 2). Profile A (top panel), a typical 00 LT solar minimum equatorial ionosphere, shows more backscatter from vertically inclined rays ( $\sim 44\text{--}75^\circ$ ) than at lower elevation angles, which is similar to the ray tracing simulation in Figure 4 (top panel) derived from Profile C at noon with medium *f<sub>oF2</sub>*. Orthogonality ( $\alpha \leq 1^\circ$ ) from these vertical rays, is concentrated nearer to the radar, not detectable beyond 500 km ground range. From lower elevation rays, the curved region depleted of orthogonality ( $\alpha \leq 5^\circ$ ) emanates further in ground range at  $\approx 600$  km from the simulated radar. Due to poor orthogonality for Ionospheric Profile A at midnight with low *f<sub>oF2</sub>*, only a half hop propagation after 2,000 km ground range is possible. In contrast, there is more backscatter in Profiles F (middle panel) and H (bottom panel) of Figure 5, representing typical 06 and 18 LT solar maximum ionospheres, respectively. Both panels show similar one and a half hop propagation to the simulation for Bo Njala in Figure 4 (top

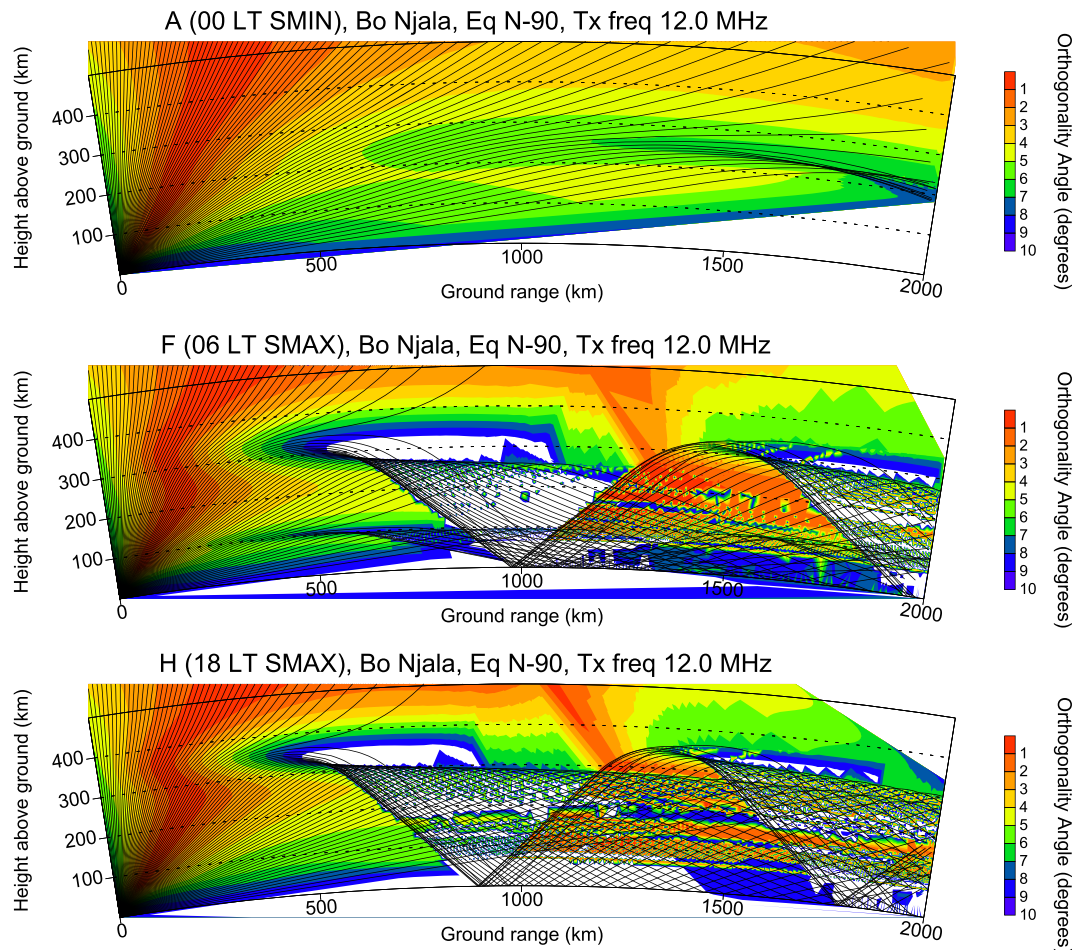


**Figure 5.** Same as Figure 4 except that it is for Bo Njala location only and the Ionospheric Profiles A, F, and H parameters are used as shown in the top, middle, and bottom panels, respectively.

panel). Except that for Profile F, the patches of backscatter from rays reflecting off the ground to the ionosphere appear further out from the radar location at half hop  $\approx 1,000$  km and one and a half hop  $\approx 1,950$  km ground range. While for Profile H, the patches of backscatter appear closer to the simulated radar location at half hop  $\approx 900$  km and one and a half hop  $\approx 1,750$  km ground range compared to Profile C in Figure 4 (top panel). The marked differences in where the half hop and one and a half hop reflect off the ground may be controlled by the *E* region critical frequency ( $f_{oE}$ ). In this case, Profile H has a lower  $f_{oE}$  value than Profiles F and C (Figure 4, top panel).

Figure 6 is similar to Figure 4 (top panel) except that here the transmit frequencies are, from the top to bottom panels, 12, 16, 20, and 24 MHz, respectively. The curved region, depleted of orthogonality ( $\alpha \leq 5^\circ$ ), tends to diminish with increasing frequency. This indicates that at higher transmit frequency, rays penetrate the ionosphere more and, as such, achieve orthogonality. But at lower transmit frequency, lower elevation rays are susceptible to both reflection and refraction, resulting to more orthogonality especially at lower altitudes.

Figures 4–6 clearly show that the possibility of achieving backscatter for azimuth  $90^\circ$  (east-west propagation) in the equatorial latitude will vary at different locations due to deviation of the Earth's magnetic field across radar FOV. The possibility of achieving backscatter will also be determined by the predominant ionospheric conditions and transmit frequency along with other controlling factors. As such, to determine the combinations of these radar operating parameters where achieving backscatter in a SuperDARN scenario is most feasible, we performed similar ray tracing simulations for all the possible azimuths. Backscatter observed by a SuperDARN-type radar as earlier noted is classified mainly as the ionospheric scatter, which is the main consideration of this study, and the ground scatter. In subsequent sections, we briefly consider

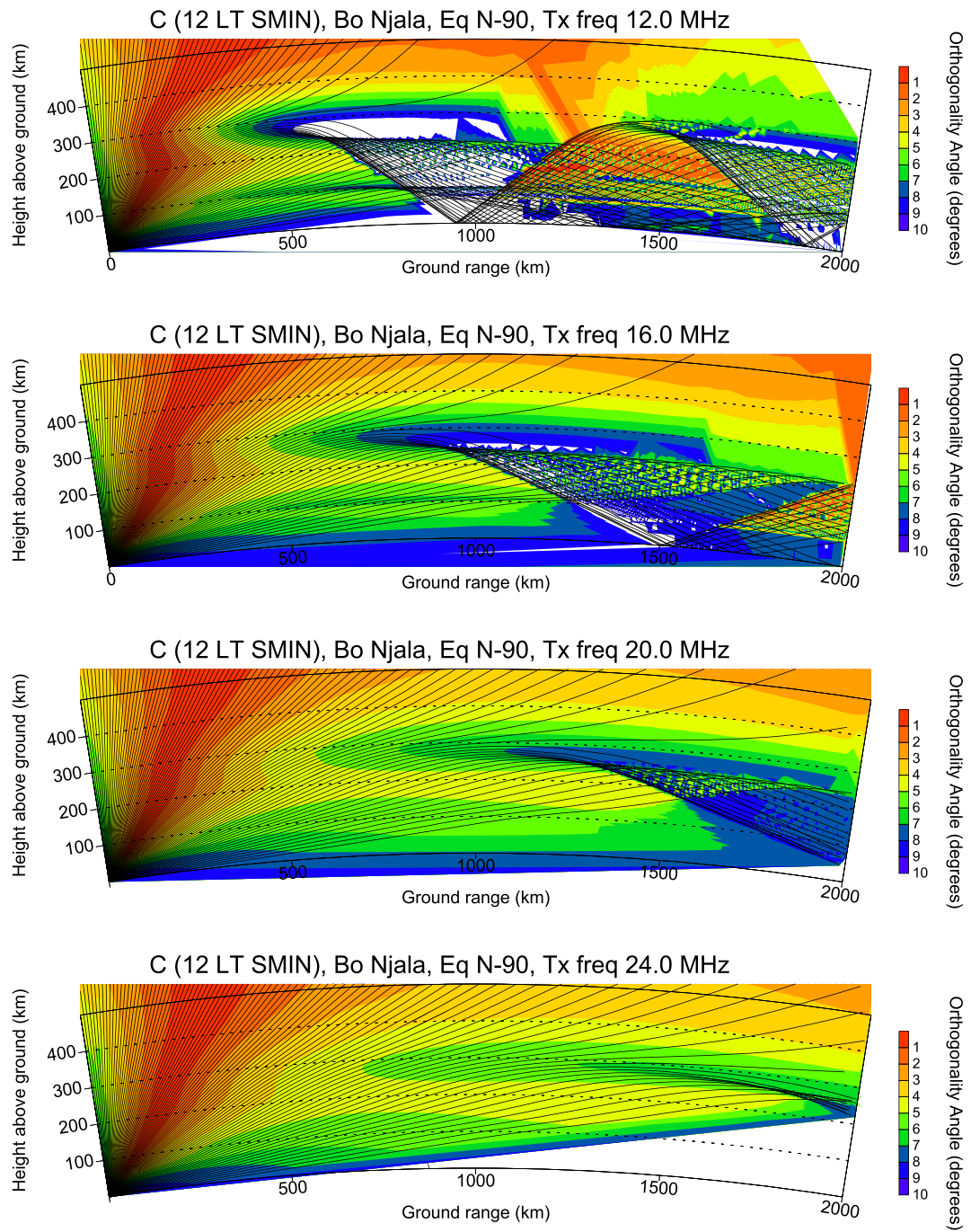


**Figure 6.** Same as Figure 4 except that it is for Bo Njala location only and the transmitted frequencies are 12, 16, 20, and 24 MHz as shown in first, second, third and, fourth rows from top, respectively.

ground scatter then report the results of the analysis for these controlling factors in respect of the likelihood of achieving orthogonality for ionospheric scatter.

### 3.1. Ground Scatter Evaluation

The primary observations of the existing SuperDARN radars are ionospheric and ground scatter (Chisham et al., 2007; Nishitani et al., 2019; Ribeiro et al., 2011). Ground scatter as earlier mentioned is due to backscattering from the Earth's surface. Here, we consider the ranges where ground scatter features are likely to be observed. Such ground scatter features with respect to present ray tracing analysis are a function of the ionospheric model and transmit frequency but independent of the radar location. As such, the Bo Njala location

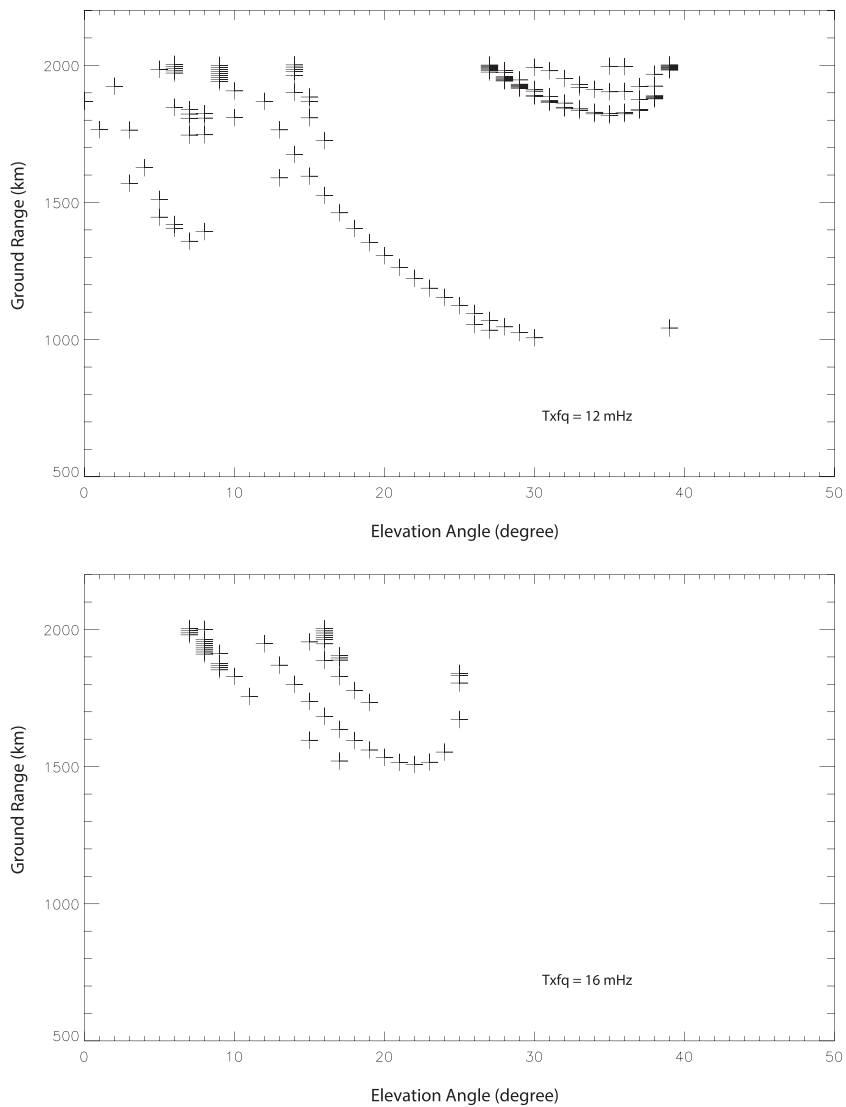


**Figure 7.** Ground scatter evaluation as a function of ground range and elevation angle for transmit frequency of 12 MHz (top panel) and 16 MHz (bottom panel) using the Ionospheric Profile C (at noon with medium  $f_{oF2}$ ) for the Bo Njala simulated radar.

out of the three locations used in this study (see Table 1) has been employed for this aspect of ground scatter evaluation.

Figure 7 examines the distribution of simulated ground scatter occurrence as a function of ground range and elevation angles for the same conditions in Figure 6. As seen in Figure 6, the two higher frequencies (20 and 24 MHz) in third and fourth rows have either no ground scatter at less than 2,000 km (24 MHz) or just achieve sufficient refraction for ground scatter very close to 2,000 km (20 MHz). Therefore, Figure 7 just looks at the lower two frequencies (12 and 16 MHz) in first and second rows of Figure 6, where reflected rays have reached the ground within a ground range of 2,000 km. Here, the ground range and elevation angle information has been collected for ray points where the altitude of a raypath reaches 0 after it has reflected from the ionosphere.

Figure 7 (top panel) shows elevation angle versus ground range for ground scatter from the transmit frequency of 12 MHz and ionosphere in Figure 6 (first row). The one hop ground scatter propagation in Figure 6 (first row) can be seen in Figure 7 (top panel) to produce one hop ground scatter from the skip distance at 1,000 km, 30° elevation angle out to 2,000 km at close to 0° elevation angle. Also, a two hop ground scatter propagation from 27–40° can be seen at ranges of about 1,800–2,000 km. Figure 7 (bottom panel) provides

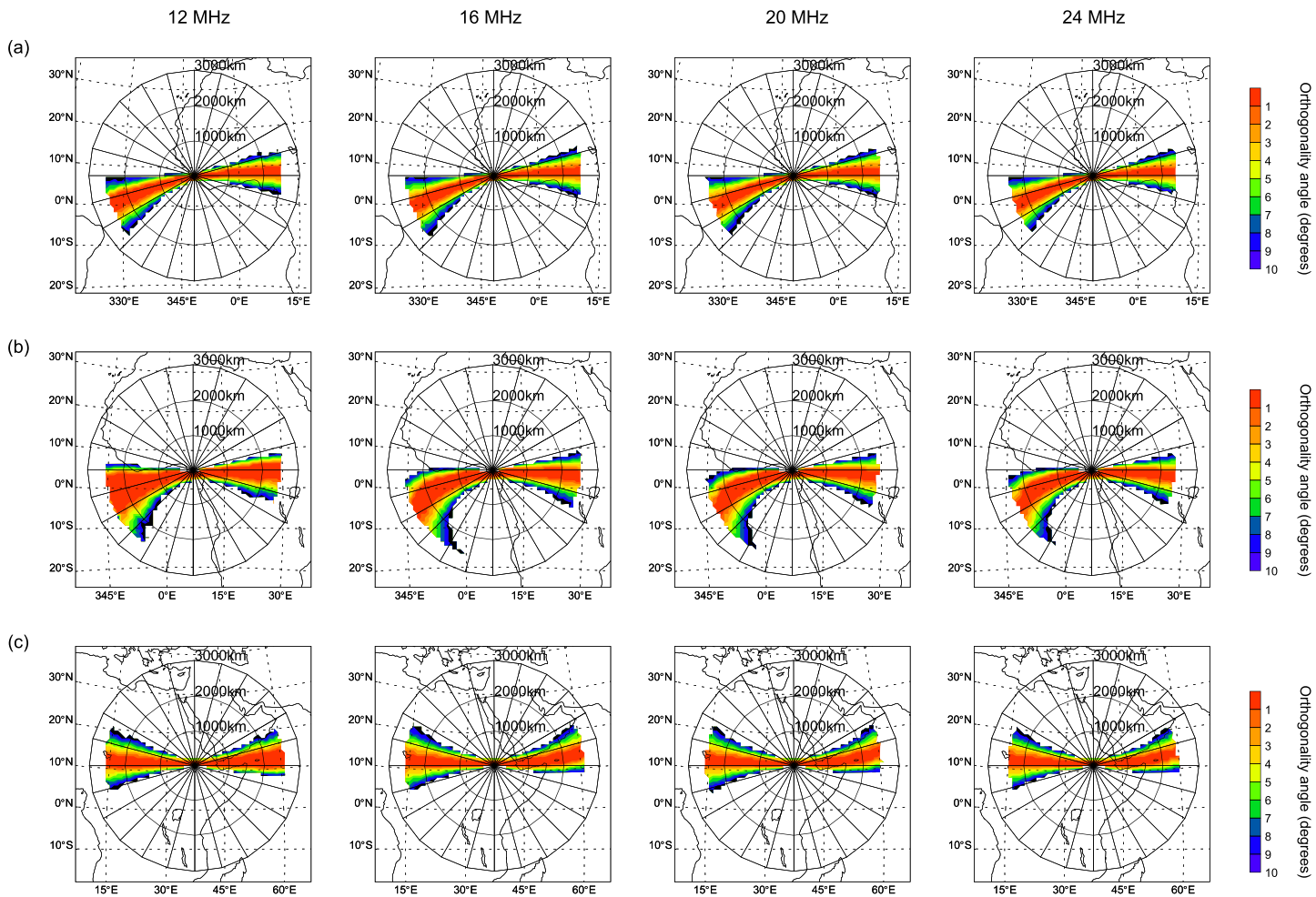


**Figure 8.** Spatial distribution of regions with perpendicularity,  $\alpha$  (color coded) between radar wave vector and the Earth's magnetic field within  $10^\circ$ . Plots derived from the Ionospheric Profile A (00 LT solar min) parameters, looking through  $1\text{--}360^\circ$  azimuths for transmit frequencies of 12 MHz (first column), 16 MHz (second column), 20 MHz (third column), and 24 MHz (fourth column). Rays propagate from the elevation angles of  $1^\circ$  to  $90^\circ$ . The rows a, b, and c represent Bo Njala, Port Harcourt, and Bahir Dar locations, respectively.

a similar analysis for transmit frequency 16 MHz, as shown in Figure 6 (second row). At 16 MHz, just one hop ground scatter propagation is produced from the skip distance at 1,500 km,  $\sim 25^\circ$  elevation angle out to 2,000 km at close to  $\sim 7^\circ$  elevation angle. The rays of larger elevation angles generate ground scatter at shorter ground range at both 12 and 16 MHz transmit frequency. Comparing the possible distribution of ground scatter described here with Figure 3 (bottom panel) indicates that for stronger ionospheres and lower transmit frequencies, we would expect ground scatter to dominate, hence our choice of 12–24 MHz for the equatorial radar.

### 3.2. Azimuth Distribution of Simulated Backscatter

We have performed ray tracing as demonstrated in section 3 between  $1^\circ$  and  $360^\circ$  azimuth for 12, 16, 20, and 24 MHz radar operating frequency at each radar location. The ray tracing for each azimuth scanned through the elevation angles between  $1^\circ$  and  $90^\circ$  at  $0.1^\circ$  steps. The calculated performance characteristics, comprising orthogonality values with their latitude, longitude, group path, ground range, and altitude, were stored for each transmit frequency, simulated radar and ionospheric profile. The data were then binned by orthogonality ( $\alpha \leq 10^\circ$ ), with emphasis on the regions where  $\alpha \leq 1^\circ$  in ensuing analysis as before. The altitude range is set between 100 and 500 km, a region that encapsulates the *E* and *F* region ionosphere, while the maximum range from the simulated radar location is set at 2,500 km. Uncertainties associated with the raypath and the regions indicated as perpendicular with the geomagnetic field increase with increasing ground range. So results obtained further from 2,500 km are harder to simulate accurately, although radar

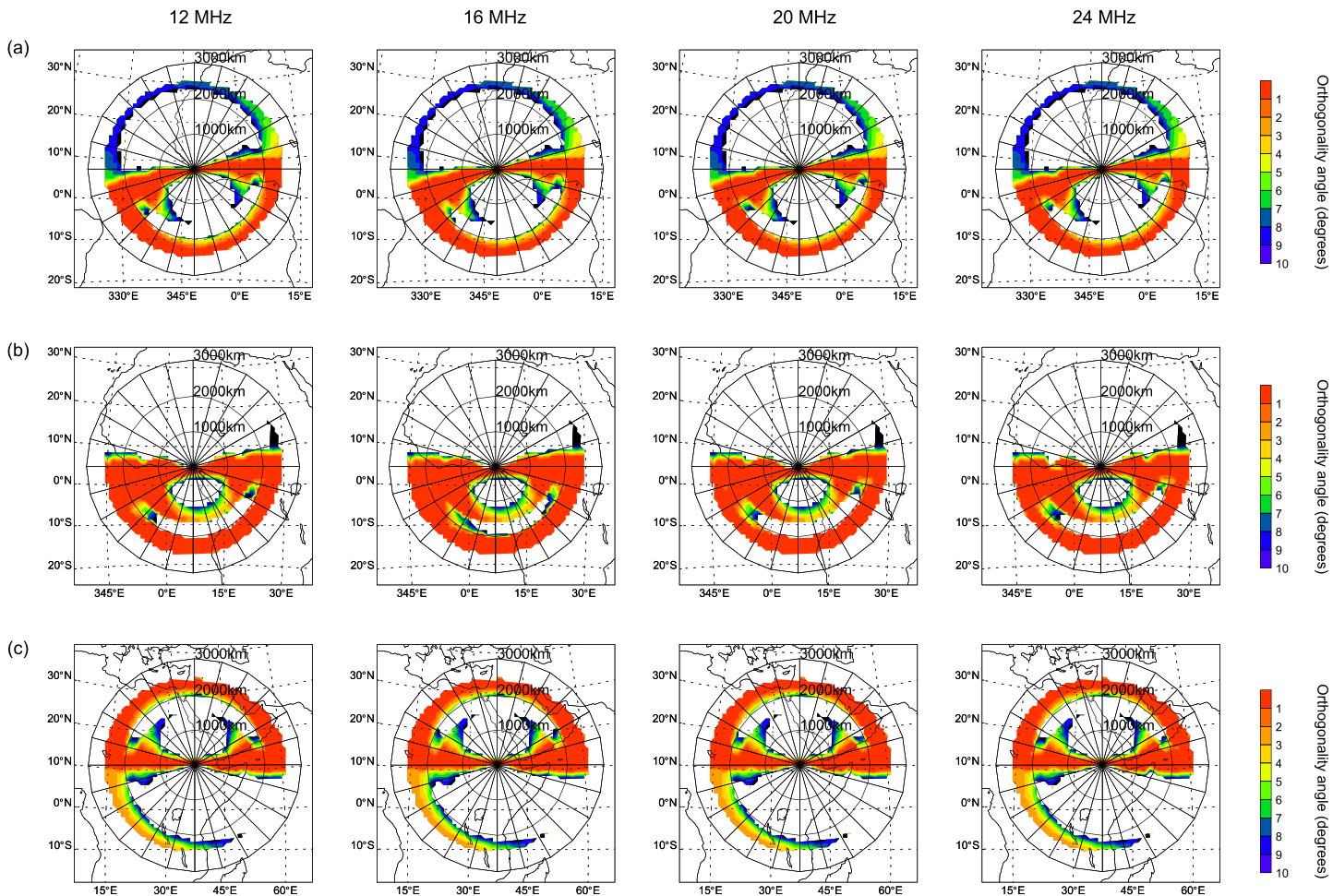


**Figure 9.** Same as Figure 8 but using Ionospheric Profile C (12 LT solar min) parameters.

backscatter is still expected from further ranges. The binned data are then gridded in steps of  $1^\circ$  of latitude and longitude. In each grid, the minimum value of orthogonality is selected and the resulting data for the grids presented in geographic stereographic coordinates in Figure 8, where radar ranges of 1,000, 2,000, and 3,000 km from the simulated radar site are marked with concentric circles (corresponding to typical ground distances in Figures 4–6, and radar azimuth is indicated radially from the radar site every  $15^\circ$ ). The minimum value of orthogonality recorded in each latitude-longitude cell is color coded with deep red indicating regions where  $\alpha \leq 1^\circ$ , which is synonymous with where there is a maximum likelihood of achieving backscatter in a SuperDARN radar. The top, middle, and bottom rows represent the Bo Njala, Port Harcourt, and Bahir Dar simulated radars, respectively, while the first, second, third, and fourth columns represent 12, 16, 20, and 24 MHz radar operating frequencies. Figures 8 and 9 are derived using Ionospheric Profiles A and C, respectively, and the same procedure has been replicated for all the ionospheric profiles.

As seen in Figure 8, the pronounced regions with simulated backscatter in each simulation are predominantly within the east-west azimuthal direction depicting a “bow-tie” shape. In Figure 8 (top panels), representing Bo Njala radar, the region with good orthogonality in 12, 16, 20, and 24 MHz radar operating frequencies spreads across all radar ranges from close to the radar out to  $\approx 2,500$  km between radar azimuth of  $75\text{--}100^\circ$  in the eastward direction and  $235\text{--}260^\circ$  in westward axis. Here, the azimuthal extent with good orthogonality is  $\sim 25^\circ$  in both eastward and westward direction. The sloped “bow-tie” feature is linked to the geometry of the Earth’s magnetic field over the Bo Njala FOV (see Figure 1).

The spatial distribution of backscatter for the Port Harcourt radar (Figure 8, row b) follows similar pattern to Bo Njala, except that the azimuthal band in each of the transmit frequency covers  $80\text{--}105^\circ$  in the eastward direction, which is  $\sim 25^\circ$  wide and correspondingly is  $230\text{--}270^\circ$  in the westward direction. At Port Harcourt,

the azimuthal extent with good orthogonality in the westward direction broadened with increasing radar ranges, covering more northward and southward azimuths than at Bo Njala. The “bow-tie” configuration tilts horizontally, spreading out in a curve southward especially at 16, 20, and 24 MHz transmit frequencies. This feature is also due to the geometry of the Earth’s magnetic field over Port Harcourt FOV as exemplified in Figure 1. On the other hand, the simulation of spatial distribution for the Bahir Dar radar, as seen in Figure 8 (bottom panels), is similar to Bo Njala and Port Harcourt radars. Here the radar azimuth covers 70–95° eastward and 255–285° westward, which represents ~25° and ~30° azimuthal coverage in eastward and westward direction respectively. The “bow-tie” feature shifts northward, spreading further away from the simulated radar site in a curve shape in all the four transmit frequencies as a result of the geomagnetic field alignment.

Figure 9 is similar to Figure 8 but for the Ionospheric Profile C at noon with medium *f<sub>oF2</sub>*. Figure 9 (top panels), shows the simulation for Bo Njala at transmit frequencies of 12, 16, 20, and 24 MHz. Simulated backscatter distribution for Profile C, Bo Njala, similar to Profile A at midnight with low *f<sub>oF2</sub>*, depicts a “bow-tie” covering all radar ranges from the radar location out to ≈2,500 km between radar azimuth of 75–100° to the east and 235–260° to the west. Also, we see a band of orthogonality at a distance of ~2,200 km radar range for all radar azimuthal angle, but with a better orthogonality in the southward axis. This orthogonality band is seen at 12, 16, 20, and 24 MHz transmit frequencies. Such band of orthogonality at ~2,200 km away from the simulated radar position might not be precise given that ray tracing simulations perform better at close ranges. The altitude where this band of orthogonality originates is much higher at a 24 MHz transmit frequency than at 12 MHz.

Azimuthal geographic distribution of orthogonality for Port Harcourt simulated radar (Ionospheric Profile C at noon with medium *f<sub>oF2</sub>*) shown in the second row of Figure 9 is similar to the Bo Njala radar. Here, we see a similar “bow-tie” characteristics covering all radar ranges from close to the radar out to ≈2,500 km between radar azimuth of 75–105° and 225–275° in the eastward and westward direction, respectively. Also, the band of orthogonality ( $\alpha \leq 1^\circ$ ) appears at distance of ~1,500 and ~2,200 km, more in the south azimuth than in the north azimuth. This band of orthogonality as noted earlier, originates from high altitude.

Bahir Dar simulated radar for Profile C (see Figure 9, bottom panels) follows the same pattern of azimuthal geographic distribution of orthogonality as Port Harcourt and Bo Njala radars. However, the “bow-tie” feature of Bahir Dar radar covers radar azimuth of 70–95° in the eastward direction and 255–285° in the westward direction, while its band of orthogonality appears at a distance of ~2,200 km for azimuthal angles to the north. Similar to Port Harcourt and Bo Njala simulated radars, Bahir Dar radar shows ~25° azimuthal extent with good orthogonality in the east-west direction.

The signature of Earth’s magnetic field geometry is apparent in the azimuthal spatial distribution as shown in Figure 9 across the FOV of the three simulated radars. The magnetic field inclination (see Figure 1) is southward at Bo Njala and Port Harcourt but northward at Bahir Dar. Likewise, the slight east-west distortion seen in Bo Njala simulated backscatter distribution also corresponds with the shape of magnetic declination over the Bo Njala radar FOV.

### 3.2.1. Near-Vertical Spatial Distribution

The spatial distributions of rays propagating with elevation angles between 45° and 90° are now considered in more detail. Figure 10 represents a zoomed-in version of Figure 9 but only for elevation angles of  $\delta > 45^\circ$ , where panels (a), (b), (c) are for Bo Njala, Port Harcourt, and Bahir Dar radars, respectively. The orthogonality distribution at Bo Njala (at the magnetic equator) peaks vertically. In contrast, Port Harcourt (south of the magnetic equator) peaks to the south, with Bahir Dar peaking slightly north. As previously pointed out, the distortion of the geomagnetic field declination angle over the Bo Njala, Port Harcourt, and Bahir Dar FOVs explains the slope in the spatial distributions between the east and west azimuths.

The spatial distribution of the near-vertical propagation is mainly governed by the geometry of the Earth’s magnetic field; as such, it is not strongly controlled by the ionospheric plasma characteristic compared with propagation from lower elevation angles. In practice, a near-vertical ionospheric radar experiment could be applied for studying the structure and vertical velocity of EEJ over the African equatorial region.

Simulations for the azimuthal spatial distribution for lower elevation propagation as well as the performance of the near-vertical propagation of the other ionospheric profiles (not presented here) follow the same

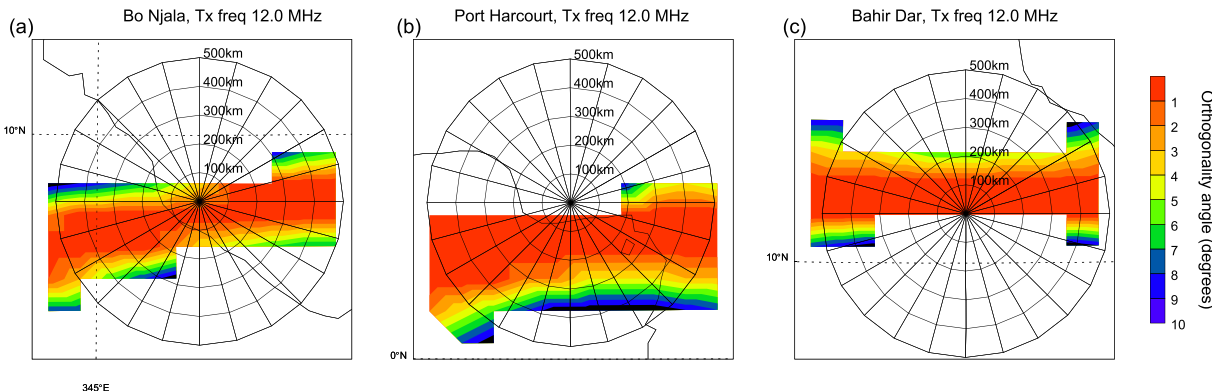


**Figure 10.** Spatial distribution of regions with perpendicularity (color coded) between radar wave vector and the Earth's magnetic field within  $10^{\circ}$ . Plots derived from the Ionospheric Profile C (12 LT solar min) parameters for near-vertical elevation angles ( $45\text{--}90^{\circ}$ ), looking through  $1\text{--}360^{\circ}$  azimuths for transmit frequency of 12 MHz. Panels (a), (b), and (c) represent Bo Njala, Port Harcourt, and Bahir Dar locations, respectively.

pattern as for Profile A in Figure 8 and Profile C in Figures 9 and 10. In the subsequent sections, we evaluate the simulated radars performance as a function of elevation angle, ground range, and altitude.

### 3.3. Elevation Angle Distribution

The analysis of the backscatter occurrence as a function of elevation angles for all the eight representative ionospheric profiles used in this study is presented here. The azimuth is restricted to  $75\text{--}100^{\circ}$ ,  $80\text{--}105^{\circ}$ , and  $70\text{--}95^{\circ}$  from the north geographic coordinate for Bo Njala, Port Harcourt, and Bahir Dar simulated radars, respectively. We evaluate only the east FOVs in the subsequent analysis since the east and west azimuthal spatial performance were very similar. For each transmit frequency (12, 16, 20, and 24 MHz), we performed a ray tracing using the appropriate azimuths from which orthogonality has been determined. The orthogonality values where  $\alpha \leq 1^{\circ}$  are selected and binned at altitudes between 100 and 500 km and limited to a ground range of 2,500 km.

As shown in Figure 11, the Ionospheric Profile A (00 LT solar minimum) in the first column exhibits similar orthogonality performances at elevation angles between  $1^{\circ}$  and  $75^{\circ}$  for the Bo Njala simulated radar. Backscatter occurs from the horizontal elevation angles in 12, 16, 20, and 24 MHz radar frequencies. The occurrence level of 12 MHz for Bo Njala radar is slightly better than other frequencies at elevation angle between  $1^{\circ}$  and  $18^{\circ}$ . This occurrence level is likely from a half hop scatter at high altitude as exemplified in Figure 5a. Low elevation angles for Port Harcourt and Bahir Dar simulated radars (second and third rows of Figure 11) performed similarly to Bo Njala, but the extent of elevation angles with orthogonality occurrence for Port Harcourt and Bahir Dar radars is  $1\text{--}50^{\circ}$  and  $1\text{--}68^{\circ}$ , respectively.

Figure 11 (second column) represents simulations for Ionospheric Profile B, a typical 06 LT solar minimum equatorial ionosphere, at the three radar locations. Simulations for Bo Njala show enhanced backscatter probability for 12 MHz transmit frequency from elevation angle of  $10^{\circ}$  and at about  $4^{\circ}$  for 16 MHz. Higher frequencies follow the same trend except that backscatter occurs from  $1^{\circ}$  horizontal elevation angle. Also, a rapid decrease in occurrence appears at  $\sim 24^{\circ}$  elevation angle for 12 MHz transmit frequency. This decrease was slight for 16 MHz and starts at  $\sim 14^{\circ}$  elevation angle, while for 20 and 24 MHz this feature is not obvious. The backscatter from more vertical elevation angles ( $\sim 45\text{--}80^{\circ}$ ) follows the same trend regardless of the transmit frequency. As stated earlier, backscatter from such elevation angles is mainly due to the geomagnetic field orientation rather than due to the influence of refraction associated with ionospheric plasma density distributions. The vertically aligned ( $45\text{--}80^{\circ}$ ) rays propagate through the ionosphere, achieving orthogonality where ray vectors are in the orientation that allow them to achieve orthogonality as illustrated in Figure 2 and in ray tracing shown in Figures 4–6. The Port Harcourt simulated radar performance as function of elevation angle is similar to Bo Njala similar except that there is no backscatter beyond  $\sim 55^{\circ}$  elevation angle, an indication of poor performance of near-vertical elevation angles. At Bahir Dar, the elevation angles performances follow the same trend as Bo Njala and Port Harcourt radars but with a poorer performance for near-vertical elevation angles when compared to Bo Njala radar and a better performance compared to Port Harcourt radar. There is no backscatter for Bahir Dar radar beyond  $\sim 70^{\circ}$  elevation angle.

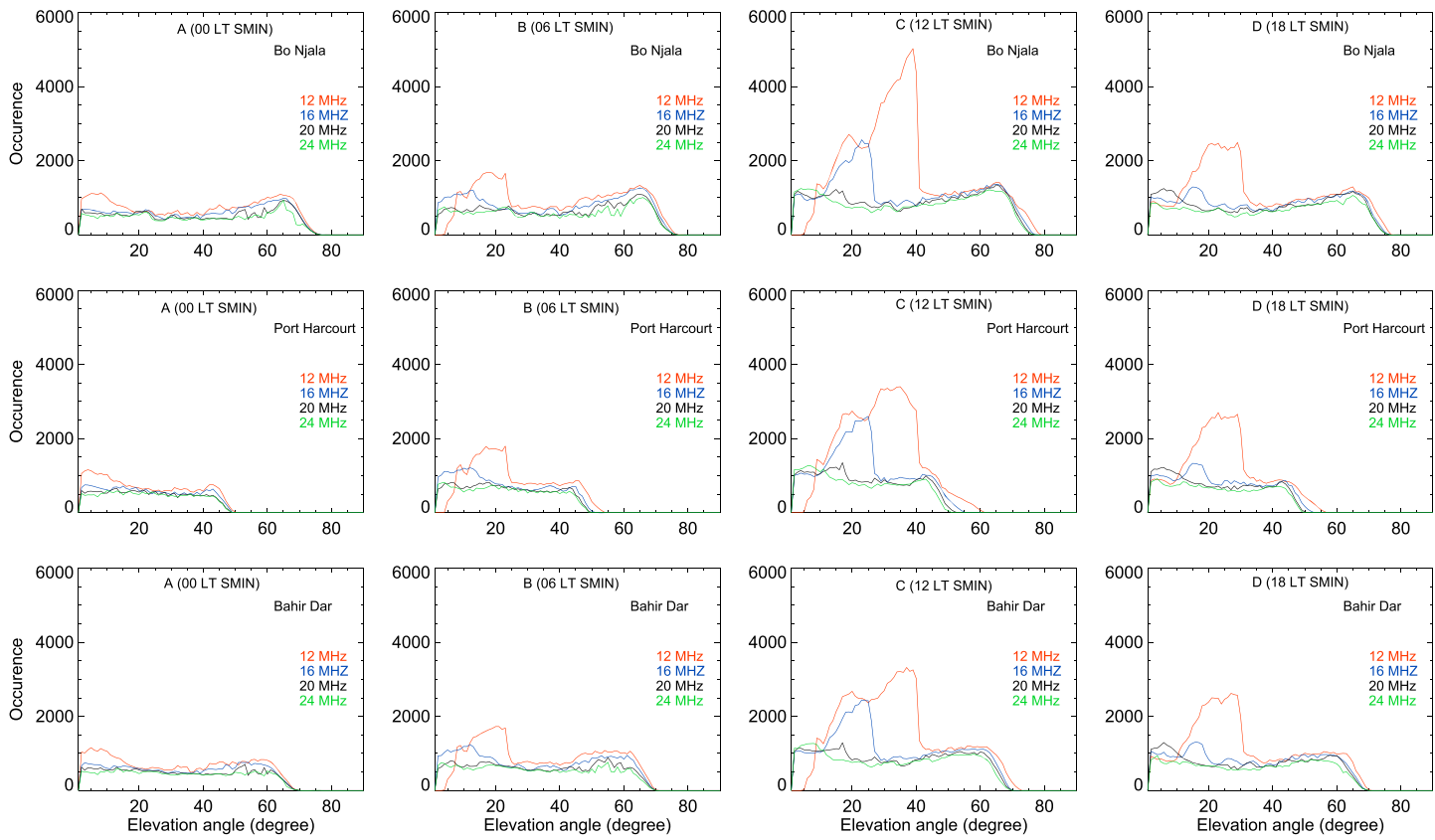


**Figure 11.** Evaluation of orthogonality ( $\alpha \leq 1^\circ$ ) as a function of elevation angle for transmit frequencies 12 MHz (red), 16 MHz (blue), 20 MHz (black), and 24 MHz (green). Plots derived from the solar minimum Ionospheric Profiles A (column 1), B (column 2), C (column 3), and D (column 4) parameters, looking through designated east-west azimuths measured from north geographic coordinate, top panels (Bo Njala, 75–100° azimuth), middle panels (Port Harcourt, 80–105° azimuth), and bottom panels (Bahir Dar, 70–95° azimuth).

Profile C, a 12 LT solar minimum representative equatorial ionosphere, is shown as Figure 11 (third column). Backscatter occurrence, similar to Profile B, is observed in 12 MHz frequency starting from elevation angle of  $\sim 10^\circ$  and from  $\sim 4^\circ$  in 16 MHz, while at higher frequencies backscatter starts from horizontal elevation. A slope in occurrence is noticeable at  $\sim 24^\circ$  elevation angle from rays transmitted at 12 MHz, which is similar to scatter occurrence for Profile B. It then steadily increased up to  $41^\circ$  elevation angle, at which it rapidly decreased to  $10^\circ$  elevation angle level. The slope for 16 MHz radar frequency is seen at  $\sim 24^\circ$  elevation angle. Simulated backscatter for near-vertical rays ( $\sim 45$ – $80^\circ$ ) follows the same trend regardless of the radar frequency. Port Harcourt and Bahir radars follow similar elevation angle performance as Bo Njala radar, except that there is no backscatter occurrence beyond  $\sim 55^\circ$  elevation angle for Port Harcourt and  $\sim 70^\circ$  elevation angle for Bahir Dar. The obvious increase in occurrence level of Ionospheric Profile C at noon with medium  $f_{oF2}$  compared with B at dawn with low  $f_{oF2}$  is due to the enhanced electron density associated with 12 LT diurnal ionosphere. Thus, for Profile C, we see backscatter from the lower elevation angle half hop *E* region and one and a half hop *F* region dominating especially for lower transmit frequencies. The propagation resulting to this feature is illustrated in Figure 6.

The Ionospheric Profile D (18 LT solar minimum) is presented in the fourth column of Figure 11. The variation in backscatter occurrence for Profile D follows similar trends observed in Profile C at noon with medium  $f_{oF2}$ , because they have comparable ionospheric electron density. However, backscatter occurs from the horizontal elevation angles as seen in Profile A with the occurrence level for 12 MHz slightly better than for other frequencies at elevation angle between  $\sim 11^\circ$  and  $32^\circ$ . The similarity in the occurrence of backscatter from horizontal elevation angle in Profiles A and D for rays transmitted at 12 MHz is as a result of depletion in electron density in *E* region ionosphere that characterizes 00 and 18 LT typical ionospheres compared to *E* region electron density enhancement of 06 and 12 LT ionospheres. A sharp fall in the level of backscatter

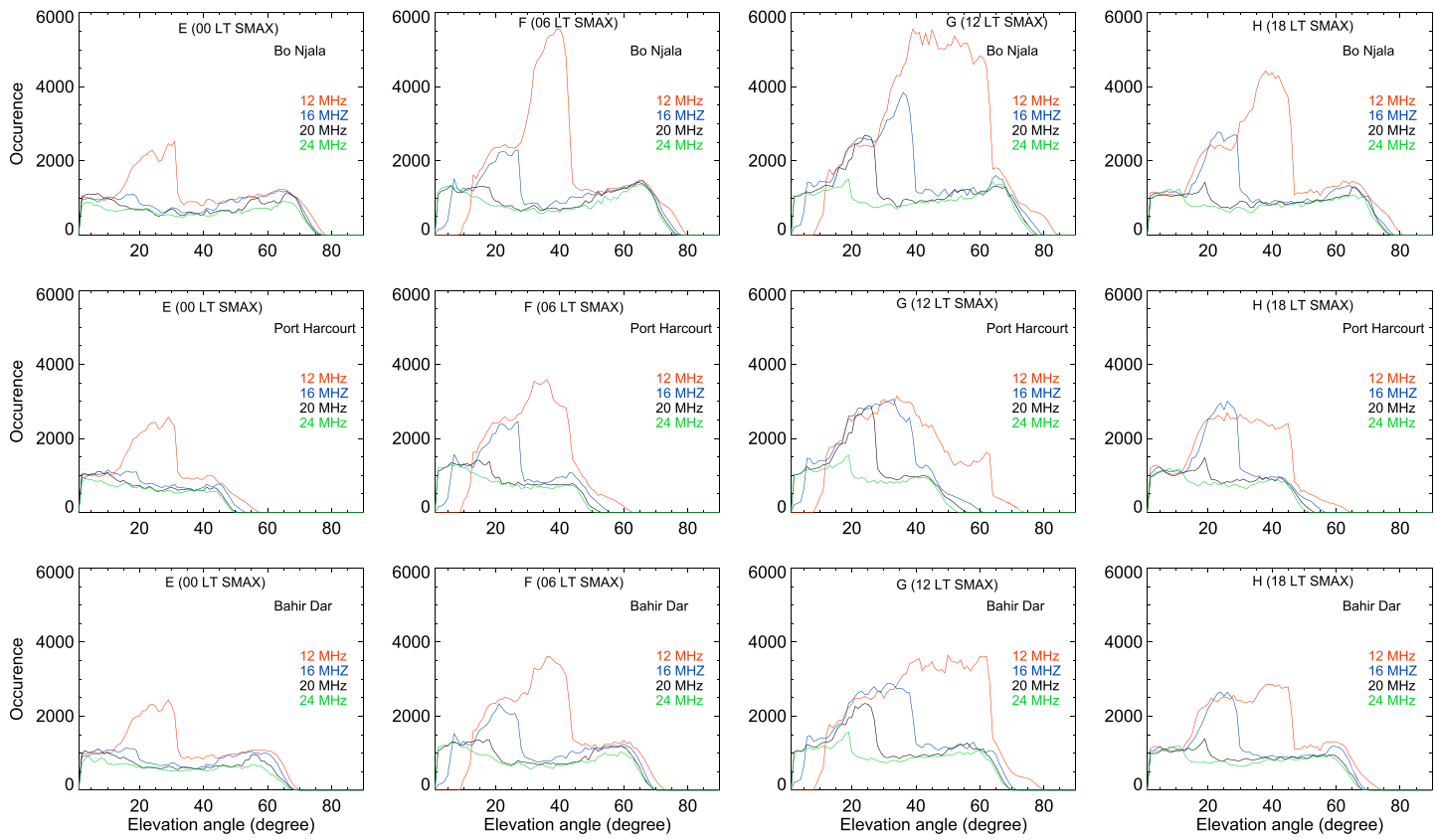


**Figure 12.** Same as Figure 11 but using solar maximum Ionospheric Profiles E (column 1), F (column 2), G (column 3), and H (column 4) parameters.

occurrence appear at  $\sim 32^\circ$  elevation angle for 12 MHz and at  $\sim 20^\circ$  elevation angle for 16 MHz radar transmit frequency. The rapid decrease in the level of backscatter occurrence that we see for rays transmitted at 12 and 16 MHz frequencies, which is similar to Profiles B and C previously discussed, may be associated with hop propagation and Pedersen rays as seen for example in Figure 6.

In Figure 12, the evolution of orthogonality occurrence with respect to the elevation angles in 12, 16, 20, and 24 MHz transmit frequencies for Ionospheric Profiles E, F, G, and H are presented, respectively, in columns 1 to 4 for Bo Njala, Port Harcourt, and Bahir Dar simulated radars, respectively, shown in the row panels, in the same format as Figure 11. In Profile E (00 LT solar maximum), the orthogonality occurrence for Bo Njala radar originates from onset up to  $\sim 76^\circ$  elevation angle across 12, 16, 20, and 24 MHz transmit frequencies. However, 12 MHz transmit frequency has more scatter from elevation angles between  $\sim 11^\circ$  and  $32^\circ$  than in 16, 20, and 24 MHz. The trend we see here is similar to what we saw for Profile A, which is also a typical 00 LT ionosphere. Here, as expected, there is more backscatter because the ionosphere being a typical solar maximum ionosphere is stronger. Also, for Bo Njala, the near-vertical scatter varies similarly from elevation angle of about  $45\text{--}76^\circ$  for all the transmit frequencies. Similar performances are observed for Port Harcourt radar in the second row and Bahir Dar radar in the last row but the vertical propagation only occurred from elevation angles between  $\sim 45\text{--}55^\circ$  and  $\sim 45\text{--}70^\circ$ , respectively.

Profile F, a 06 LT solar maximum typical equatorial ionosphere, in Figure 12 (second column) shows orthogonality occurrence for Bo Njala, Port Harcourt, and Bahir Dar radars in top, middle, and bottom rows, respectively. At Bo Njala, backscatter occurs from  $\sim 10^\circ$  elevation angle for 12 MHz, while in 16 MHz it starts from  $\sim 5^\circ$  but originates from onset in 20 and 24 MHz transmit frequencies. The 12 MHz frequency has dominant occurrence from elevation angles between  $\sim 11^\circ$  and  $44^\circ$  compared to other frequencies. It increased from about  $11^\circ$  to  $\sim 24^\circ$ , decreased slightly and then increased steadily until an abrupt fall to  $\sim 11^\circ$  level at  $44^\circ$  elevation angle. This again demonstrates the trend we have seen so far, where high altitude half hop scatter dominates for weaker ionospheres, illustrated in Figures 5 and 6, with lower elevation angle half hop E region and one and a half hop F region scatter becoming dominant for stronger ionospheres and lower

frequencies. The near-vertical propagation from elevation angle of about 45–80° follows the same trend for all the transmit frequencies. The performances of Port Harcourt and Bahir Dar radars are similar to Bo Njala radar. However, at Port Harcourt, the vertical propagation is small scale, occurring only in elevation angles from ~45–60° for all transmit frequencies but stretching further between ~45° and 72° elevation angles for the Bahir Dar radar.

The performance characteristics during a 12 LT solar maximum representative equatorial ionosphere (Profile G) is presented in Figure 12 (third column). Profile G shares similarities with Profiles F and C, but the magnitude of backscatter occurrence for all the transmit frequencies and radars is seemingly largest in Profile G due to its intense ionospheric density characteristics compared to other representative profiles. For the Bo Njala radar, backscatter is noticeable from elevation angle of ~10° for 12 MHz and from ~4° at 16 MHz. At 12 MHz, there is an upward slope from elevation angle of ~10° up to ~27°, where it slightly decreased before peaking at ~40°. It fluctuates at the peak level and then falls to the 10° level at ~65° elevation angle. The 16 MHz followed the same trend, although it slightly performed better than 12 MHz between 11° and 27°, then dropped to 10° level at ~27°. Unlike in other profiles, there is obvious initial upward slope in 20 and 24 MHz and rapid fall at ~27° and ~20°, respectively. The backscatter population from the lower elevation angle half hop *E* region and one and a half hop *F* region and again for lower transmit frequencies explains the variation of scatter in Profile G at noon with high *f<sub>oF2</sub>*. Similar plots to Figure 6 not presented here confirm this assertion. The Port Harcourt radar followed same trend as Bo Njala radar except that there is no backscatter occurrence beyond ~71° elevation for 12 MHz and ~60° for other frequencies. At Bahir Dar, the elevation angle performance is similar to Bo Njala and Port Harcourt but there is no occurrence of backscatter beyond ~80° elevation angle for 12 MHz and ~70° for other frequencies.

Finally, in Profile H (18 LT solar maximum), the backscatter occurrence for Bo Njala radar originates from horizontal elevation angle for all the transmit frequencies despite the relatively high *f<sub>oF2</sub>* of this profile. This feature, also seen in similar 18 LT ionosphere (Profile D), could be as a result of Profile H relatively small *f<sub>oE</sub>* compared with Profile G. In 12 MHz, there is an increase of occurrence from elevation angle of ~10° up to ~27°. This is followed by a slight decrease then increase to a peak level before falling to ~10° elevation angle level at ~44°. The near-vertical rays from elevation angle of about 45–80° vary similarly for all the transmit frequencies. The orthogonality occurrences for Port Harcourt and Bahir Dar radars vary same as Bo Njala radar. But at Port Harcourt, there is no occurrence beyond elevation angle of ~60°, while at Bahir Dar orthogonality occurrence terminated at ~72°. As suggested earlier, the rapid fluctuation in the level of backscatter occurrence seen in all the solar maximum typical ionospheres, especially for 12 and 16 MHz frequencies could be due to multihop propagation and Pedersen rays exemplified in Figure 6.

### 3.4. Ground Range Distribution

In this section, we present in detail the simulated backscatter distributions as a function of ground range across 1° to 90° elevation angles. Figure 13, derived from the ionospheric parameters of Profiles A (top panels), C (middle panels), and G (bottom panels) for Bo Njala, shows that simulated backscatter is not distributed uniformly over the ground range in all the four transmit frequencies. To achieve Figure 13, we binned orthogonality value at ( $\alpha \leq 1^\circ$ ) and altitude between 100 and 500 km.

Figure 13 (top panels) depicts orthogonality occurrence as a function of ground range and elevation angles for the Profile A ionosphere for Bo Njala radar at transmit frequencies of 12, 16, 20, and 24 MHz. The near-vertical backscatter that originates from elevation angles of ~40–70° can be seen. This near-vertical backscatter that appears like reddish “blob,” covers from the simulated radar site to ≈500 km ground range in all the transmit frequencies. However, at lower frequencies 12 and 16 MHz, there is more backscatter than at 20 and 24 MHz. The frequency variation of backscatter is due to Ionospheric Profile A having low ionospheric density (e.g., *f<sub>oF2</sub>* is 3.9 MHz) relative to the transmit frequencies. For example, propagation for the near-vertical backscatter is typified in the top panels of Figure 5. At higher transmit frequencies there is no hop propagation so rays tend to penetrate the ionosphere producing less backscatter. Also, there is a backscatter region from the low elevation angles of ≈1° to about 40° across the transmit frequencies. Propagation from these low elevation angles produces oblique orthogonality, with the orthogonality occurring at above 2,000 km range in 12 MHz due to half hop as illustrated in Figure 5.

Profiles C and G (middle and bottom panels of Figure 13) represent stronger ionospheres, which allows us to compare ionospheric effect on the orthogonality distribution as a function of ground range and elevation angles. Here, the near-vertical backscatter is similar to Profile A at midnight with low *f<sub>oF2</sub>*, extending from

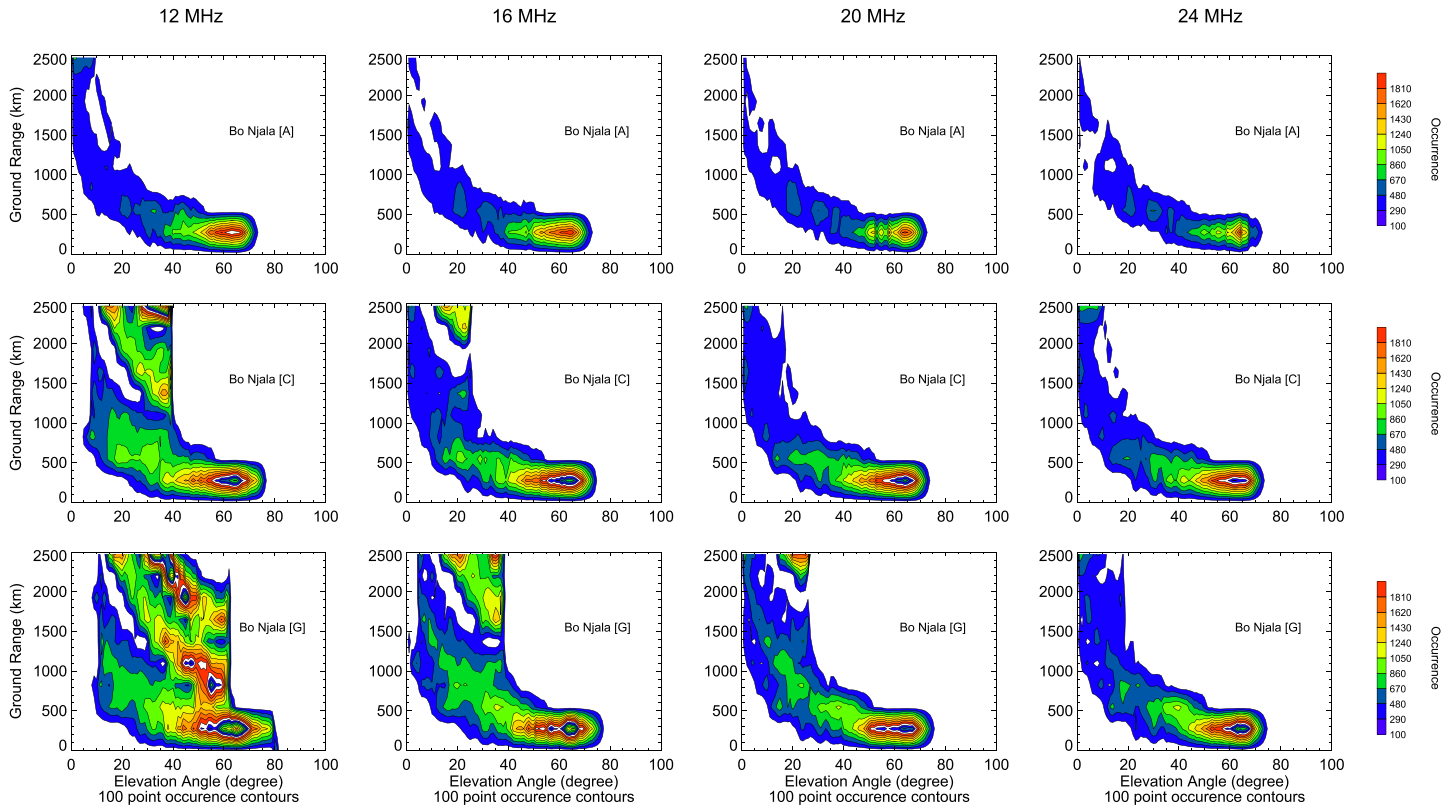


**Figure 13.** Evaluation of orthogonality ( $\alpha \leq 1^\circ$ ) as a function of ground range and elevation angles for transmit frequency 12 MHz (column 1), 16 MHz (column 2), 20 MHz (column 3), and 24 MHz (column 4). Plots derived from the ionospheric parameters of Profiles A (top panels), C (middle panels), and G (bottom panels) for Bo Njala simulated radar looking through  $75\text{--}100^\circ$  eastward azimuths measured from north geographic coordinate.

the simulated radar site to  $\approx 500$  km ground range but with no clear difference in 12, 16, 20, and 24 MHz transmit frequencies. In contrast, the low elevation angles produced more backscatter across the ground ranges in Profiles G and C than in Profile A. The increasing scatter from the *E* region half hop and *F* region one and a half hop propagation account for the more backscatter especially in the 12 MHz transmit frequency. This hop feature is demonstrated in Figures 4 and 5 and appears more at lower transmit frequencies as shown in Figure 6. Here in Figure 13, multihop features as well as Pedersen rays can be seen as the longer ground range distributions appearing from 950 to 2,500 km ground range. Also, the backscatter distribution for Profiles C and G in 12 MHz transmit frequency is different from Profile A. For example, we do not see backscatter from the horizontal elevation angle in 12 MHz transmit frequency due to large *E* region ionospheric critical frequency ( $f_{oE}$ ) associated with 12 LT ionosphere. However, at higher transmit frequencies, rays from the horizontal elevation angles as exemplified in Figure 6 penetrate the *E* region then refract in the *F* region and produce backscatter at high altitude. Thus, Figure 13 confirms that the likelihood of achieving orthogonality is not uniformly distributed in ground range but depends on the radar frequency and the elevation angle of propagation. Simulations of ground range distributions of orthogonality for Port Harcourt and Bahir Dar radars (not presented here) are similar to the Bo Njala radar.

### 3.5. Altitude Distribution

A detailed analysis of the altitude structure of orthogonality occurrence has been performed. Here we set the altitude between 1 and 500 km, which represents an altitude range that encompasses the *E* and *F* region ionospheric plasma irregularities features predominant in equatorial latitude such as sporadic *E* observed by Blanc et al. (1996) at altitude range of 100–150 km. It is also a reasonable altitude range to focus our analysis using a delineation of the EEJ region to (100–110 km in altitude) and within a few degrees of latitude at the magnetic equator (Richmond, 1973). Note that the conventional SuperDARN signal processing currently does not estimate the altitude of backscatter, although there are models, for example, by Chisham et al. (2008) and Yeoman et al. (2008) that can provide altitude information of backscatters closer to the radar.

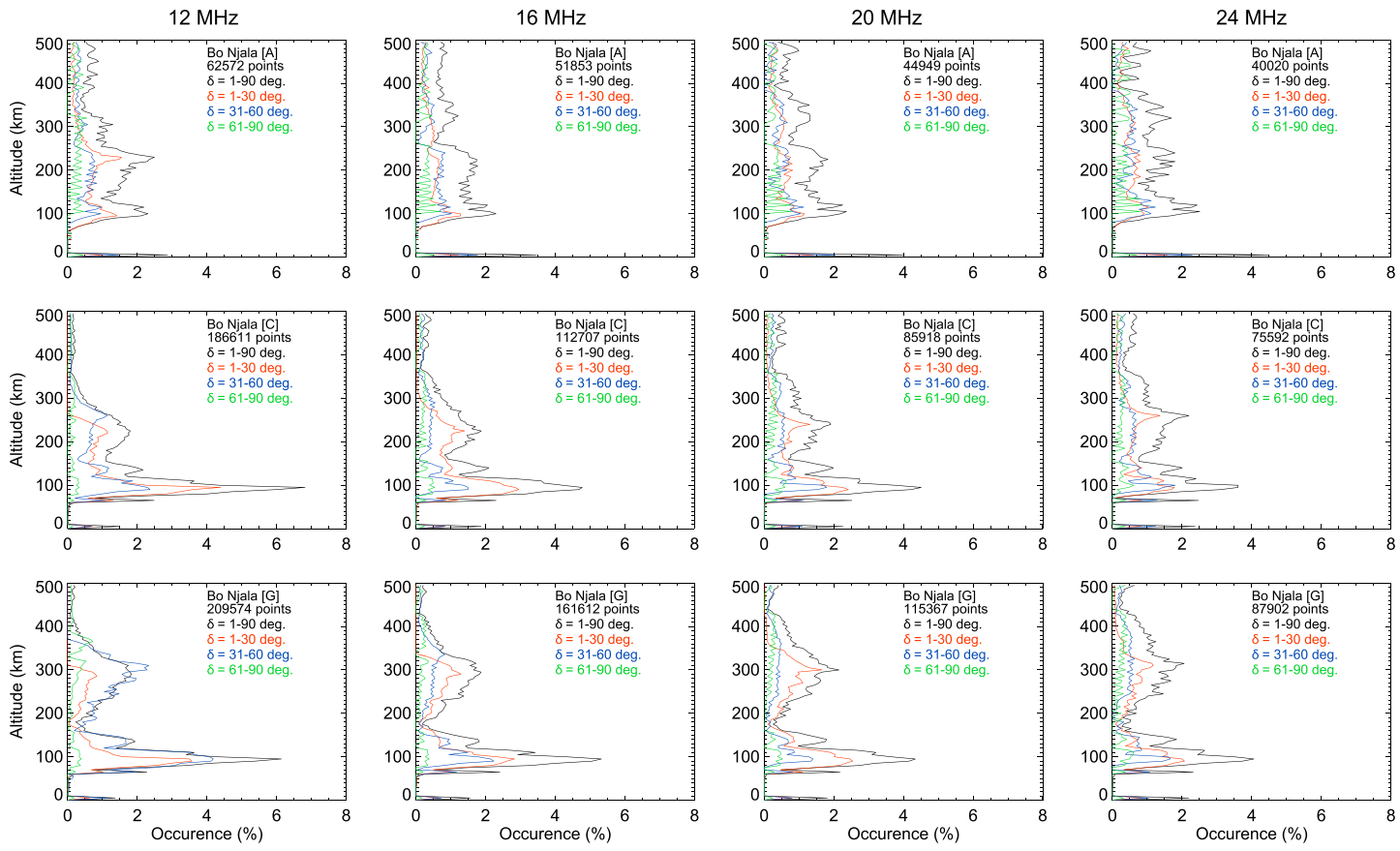


**Figure 14.** Evaluation of orthogonality ( $\alpha \leq 1^\circ$ ) as a function of altitude range  $\leq 500$  km for transmit frequencies 12 MHz (column 1), 16 MHz (column 2), 20 MHz (column 3), and 24 MHz (column 4). Plot derived from the parameters of Ionospheric Profiles A (top panels), C (middle panels), and G (bottom panels), for Bo Njala simulated radar looking through  $75\text{--}100^\circ$  azimuths from North geographic coordinate and at different classifications of elevation angles ( $\delta$ ). Altitude bins are 5 km wide.

Figure 14 depicts simulated altitude distribution of orthogonality occurrence for the Bo Njala radar, derived from the profiles A (top panels), C (middle panels) and G (bottom panels) representative ionospheres for transmit frequencies of 12, 16, 20, and 24 MHz. In Figure 14, we binned the altitude region (1–500 km) at 5 km interval, from which the total occurrence of orthogonality ( $\alpha \leq 1^\circ$ ) was recorded at each interval over the  $1\text{--}90^\circ$  elevation angle ( $\delta$ ) (black line in Figure 14). The same analysis was repeated at  $1\text{--}30^\circ$ ,  $31\text{--}60^\circ$ , and  $61\text{--}90^\circ$  elevation angle ( $\delta$ ) classifications (red, blue, and green lines in Figure 14).

As shown in Figure 14, for Profile A, significant populations of *E* and *F* region scatter are predicted at all frequencies for elevation angles less than  $60^\circ$ . The populations of *E* and *F* region scatter are even because Profile A is a weak ionosphere, a typical 00 LT ionosphere. Backscatter from the elevation angles of  $61\text{--}90^\circ$  dominates other groupings above 350 km altitude. In other words, we have seen features of such high-altitude backscatter for example, in Figures 4 and 5 from the near-vertical rays spreading out to over 1,500 km ground range as highlighted in Figure 9 (especially in 24 MHz) and Figure 13.

The altitude distributions of orthogonality for Profiles C and G, representing stronger ionospheres, are in the middle and bottom panels of Figure 14. Here, significant populations of *E* and *F* region scatter are also predicted at all frequencies. However, the populations of *E* region ionospheric scatter outweigh the *F* region because both Profiles C and G are a 00 LT representative ionosphere with a strong *E* region ionization. Similar to simulations for Profile A, backscatter originating from the elevation angles of  $61\text{--}90^\circ$  are more significant at altitudes beyond 350 km. The low elevation angles ( $1\text{--}30^\circ$ ) dominate the *E* region altitude, while the elevation angles of  $31\text{--}60^\circ$  are significant at  $\sim 300\text{--}350$  km, typical of the topside *F* region ionosphere, especially for 12 MHz transmit frequency. Simulations of altitude distributions of orthogonality for Port Harcourt and Bahir Dar radars are not presented here but follow similar trends to the Bo Njala radar.

#### 4. Discussion

Ray tracing simulations have been extensively applied for determining the contours of perpendicularity of the HF radar wave vector with the Earth's magnetic fields at high latitudes under varying ionospheric conditions prior to inception of the SuperDARN Network (Villain et al., 1984). These earlier studies formed a building block for SuperDARN. Refractive effects from ionospheric electron density distributions influence HF raypaths propagating through the ionosphere. Consequently, the spatial location where the HF wave vectors propagating through the ionosphere achieve orthogonality with the Earth magnetic field varies in latitude. The implication of this latitudinal variation is that results from HF ray tracing modeling for high latitude cannot be easily applied to equatorial latitude. Thus, this study was motivated by the need for a feasibility study toward the development of SuperDARN-like radars at equatorial latitude of the African sector given the rapid expansion of the SuperDARN Network from its original high-latitude coverage to the lower-latitude sector. In addition, the least studied equatorial African ionosphere is predominated by interesting electrodynamics such as EEJ, which is yet to be fully understood (Akala et al., 2013; Yizengaw et al., 2014) due to a lack of instrumentation to data. As such, a long-term application of SuperDARN-like HF radar technique will lead to enhanced understanding of these terrestrial plasma dynamics peculiar to equatorial ionosphere.

This study has used a modified version of the three-dimensional ray tracing computer program developed by Jones and Stephenson (1975). The modification entails the coupling of up to date IGRF magnetic field model and representative equatorial ionospheric parameters deduced from the IRI model.

Results presented in section 3.2 have clearly shown that where orthogonality can be achieved for equatorial SuperDARN-like radar will be dependent on the azimuthal direction of radar beam. In this simulation, the azimuth in the regions of 75–105° east and 230–288° west from geographic north performed best across the three simulated radars. The azimuthal extent in each of the simulated radars with good performance is ~25°. The apparent paucity of backscatter for azimuths in the north and south axes is due to the configuration of the equatorial geomagnetic field. This north-south decreasing deviation in performance appears to be higher in the azimuths lying in the Northern Hemisphere than the Southern Hemisphere, a signature possibly due to the effect of the South Atlantic Anomaly as simulations (not presented here) further down the Southern Hemisphere at latitudes up to ~15° have suggested. The superior performance of the east-west azimuthal direction relative to the north-south azimuth at different radar operating frequencies and realistic equatorial ionospheres applied in this study is primarily due to the horizontal configuration of the Earth's magnetic field at equatorial African latitude. This horizontally inclined field geometry means that the influence of refraction resulting from nonuniform electron density gradient of the ionosphere on where perpendicularity between wave vector and geomagnetic field exist is relatively small when compared with the high latitude where in order to achieve orthogonality sufficient refraction is required to bend propagating rays. This is not to say that HF wave trajectory in equatorial latitude are not susceptible to refractive effects from the ionospheric electron density distribution. Going by the azimuthal performance, to construct a SuperDARN radar in the equatorial African latitude entails a choice of radar beams with a boresite location that allows coverage of the east-west azimuthal FOV, which has shown a striking probability of achieving useful backscatter.

The 12 MHz radar frequency generally has more occurrences of simulated scatter, with the majority apparently distributed within the *E* region ionosphere from rays in the region of 1–30° elevation. Multifrequency analysis suggests that more backscatter can be achieved in the topside *F* region relative to the *E* region ionosphere by operating the radar at higher HF frequency. In such a scenario, rays from elevation angles above 30° perform well. Simulated scatter at *E* region altitudes, especially for a typical afternoon ionosphere, may be similar to features observed in radar measurement in Blanc et al. (1996), attributed to effect of solar zenith angle and the solar zenith radiation penetrating deeper into the atmosphere and producing more ionization at lower altitudes. This large-scale *E* region simulated scatter distribution is also reminiscent of the distributions found by Milan and Lester (2001) who employed the Þykkvibær SuperDARN radar measurements to study the *E* region backscatter associated with the auroral electrojets.

The elevation angles at about 1–10° produced no simulated scatter for 06 and 12 LT typical ionospheres when the rays are transmitted at 12 MHz as illustrated, for example, in Figures 11 and 12. This feature is due to comparatively large *foE* associated with the 06 and 12 LT diurnal periods. Consequently, simulated

backscatter occurrence is seen at higher transmit frequencies. There are more simulated backscatter occurrences for a typical afternoon and solar maximum ionosphere than in a realistic morning and solar minimum ionosphere, respectively. This characteristic diurnal and solar variability variations in the level of simulated scatter could be dependent on the differences in ionospheric electron densities. The different distributions of regions with the possibility of ionospheric backscatter due to variability of ionospheric plasma density profiles and local time seen here are similar to the findings in Nishitani and Ogawa (2005) for midlatitude following a similar ray tracing analysis.

Rays of lower elevation angles show features of simulated scatter, and they appear up to the maximum range of 2,500 km considered here. At such ranges ( $\geq 1,000$  km), backscatter seen, for example, in Figure 9 for higher transmit frequencies originates from the high altitude as highlighted in Figure 14. Although, features in a modeled distribution of echoes have shown to appear much further in range than in measured data and are susceptible to greater uncertainties (de Larquier et al., 2013) and are not simulated here. Therefore, in this study, backscatter above 1,000 km in ground range may be giving a less precise picture of the ground range backscatter distribution for a practical setup. Contrary to the range distribution of scatter for the lower elevation angles, scatter from the near-vertical elevation angles are confined to  $\sim 500$  km ground range away from the simulated radars. Electron density distribution may not be linked with the simulated scatter from vertical rays. Such backscatters are predominantly due to the magnetic field geometry favoring perpendicularity between radar wave vector and the Earth's magnetic field. Accurate measurements of elevation angle will be particularly important in the equatorial region, where both low and high elevation angles are likely to produce significant quantities of ionospheric backscatter.

Apart from ionospheric backscatter that requires orthogonality, SuperDARN-type radars also measure ground scatter as previously noted. Such ground scatter is useful for studying, for example, the characteristics of traveling ionospheric disturbances (e.g., Ribeiro et al., 2011). The possible ground scatter region has been predicted for 12 and 16 MHz transmit frequencies where there are multiple hop propagation modes within the ground range of 2,000 km. The likelihood of ground scatter occurrence depends on the transmit frequency and the ionosphere. For Ionospheric Profile C (at noon with medium  $f_{oF2}$ ) at transmit frequency 20 and 24 MHz, no ground scatter is predicted at ranges less than 2,000 km. Here, simulated ground scatter for the 12 MHz for Ionospheric Profile C (at noon with medium  $f_{oF2}$ ) is mainly from low elevation angles that are below  $40^\circ$  for both one and two hop propagation modes. At the 16 MHz, simulated ground scatter is between  $\sim 7^\circ$  and  $25^\circ$  elevation angles due to one hop propagation mode. At the same transmit frequency, simulated ground scatter is generated at shorter ground range for the ionospheric profiles with a medium and high  $f_{oF2}$ , typical of daytime ionosphere, which is similar to the observation noted in Nishitani and Ogawa (2005) for a midlatitude SuperDARN radar. Identifying ground scatter from ionospheric scatter in existing SuperDARN radars measurements is usually possible (Milan & Lester, 2001; Ribeiro et al., 2011). However, the algorithm used for such identification of ground scatter from ionospheric scatter for SuperDARN measurement is still not always accurate, and as such remains an issue under investigation with SuperDARN data (e.g., Ribeiro et al., 2011).

The analysis here has shown that a SuperDARN-type radar looking in the east-west azimuthal direction has the potential of achieving ionospheric backscatter at African equatorial latitudes. Therefore, such analysis needs to be considered in designing a suitable antenna for this equatorial sector. For instance, an antenna with beams that can provide a  $25^\circ$  scan coverage (one half a normal SuperDARN scan) will be a good match for the proposed radars. The front-to-back ratio has been identified as a likely limitation that HF antennas operating in the east-west azimuths will have, which needs to be considered in the design of the antenna's elevation radiation pattern, height, and separation. This would entail constructing an antenna with a large front-to-back ratio to allow for distinguishing scatter from east and west azimuths, which is crucial for a SuperDARN measurement (Custovic et al., 2011, 2013).

Most HF radars designed to study ionospheric irregularities are working at frequencies between 10 and 30 MHz and the effects of the electron density on the raypath diminish considerably with increasing radar operating frequency (Villain et al., 1984). Interesting signatures of Perderson rays at about  $8\text{--}10^\circ$  in  $E$  region and  $32\text{--}34^\circ$  in  $F$  region, half hop and one and a half hop from our simulation are features that can be validated using analysis from actual radar measurements.

## 5. Conclusion

In this paper, a ray tracing program has been applied in simulating a typical SuperDARN radar at equatorial African latitude locations. The simulated radar backscatter is consistent with the major SuperDARN radars requirement that HF rays propagate nearly perpendicular to the geomagnetic field ( $\alpha \leq 1^\circ$ ). The spatial distributions of the eight different representative ionospheric profiles studied, following this criterion, have shown that there is a likelihood of achieving backscatter in the east-west looking beams ( $25^\circ$  azimuthal range). This result shows that building a SuperDARN radar at the equatorial African latitude location would require a choice of radar boresite that allows the beams to sweep the regions covering the east-west azimuthal direction. Interestingly, this azimuthal region represents the plane where field-aligned irregularities such as EEJ flow.

The transmit frequency of 12 MHz followed by 16 MHz has the highest occurrence of simulated backscatter with majority of this distribution from the low elevation rays in the *E* region ionosphere. The middle and near vertically aligned rays achieved orthogonality better at higher frequencies of 20–24 MHz with a simulated distribution confined in the vicinity of  $\sim 500$  km ground range away from the simulated radar site. Contrarily to the vertically aligned rays, features of simulated scatter from the lower elevation angles appear up to the maximum range of 2,500 km. It should be mentioned that simulated backscatter at such 2,500 km range may not be precise since HF ray tracing produces a better result at shorter ranges. In addition, accurate measurements of elevation angle will be crucial in the equatorial region, where both low and high elevation angles are likely to produce significant quantities of ionospheric backscatter. The observations in this study will portend some implications in the antenna array construction, cost, and operation for the proposed SuperDARN radars in the African equatorial sector. Therefore, further studies on antenna array design are necessary.

Backscatter measurements of SuperDARN-like HF radars located in equatorial African latitude sector should provide important data for studying *E* and *F* region field-aligned irregularities and equatorial electrodynamic phenomena such as the EEJ. Other wide ranging terrestrial plasma research such as magnetohydrodynamic ultralow frequency waves may benefit from such data. The ionospheric profiles used in this present study are based on IRI modeled data for quiet geomagnetic period. As such, in future studies, we would employ realistic electron density profiles derived from experimental ionogram data during a quiet geomagnetic period and a disturbed period like geomagnetic storms. Also, the relationships between the vertical and latitudinal structures of backscatter seen from different simulated radar locations could be examined using ray tracing simulation.

We have shown using a HF ray tracing, a simulation of probable distributions of complex echo structures from rays at varying elevation angles in a SuperDARN radar setup. This analysis apart from its importance as a feasibility study for building HF radars at equatorial African latitudes will also provide a basis for future interpretations of results obtained from data measured from such radars.

## References

- Akala, A. O., Seemala, G. K., Doherty, P. H., Valladares, C. E., Carrano, C. S., Espinoza, J., & Oluoye, S. (2013). Comparison of equatorial GPS-TEC observations over an African station and an American station during the minimum and ascending phases of solar cycle 24. *Annales Geophysicae*, 31, 2085–2096. <https://doi.org/10.5194/angeo-31-2085-2013>
- André, R., Hanuise, C., Villain, J. P., & Cerisier, J.-C. (1997). HF radars: Multifrequency study of refraction effects and localisation of scattering. *Radio Science*, 32(1), 153–168. <https://doi.org/10.1029/96RS02987>
- Bilitza, D., Altadill, D., Zhang, Y., Mertens, C., Truhlik, V., Richards, P., et al. (2014). The International Reference Ionosphere 2012—A model of international collaboration. *Journal of Space Weather and Space Climate*, 4(A07), 14. <https://doi.org/10.1051/swsc/2014004>
- Blanc, E., & Houngninou, E. (1998). Typical disturbances of the daytime equatorial *F* region observed with a high-resolution HF radar. *Annales Geophysicae*, 16, 721–730. <https://doi.org/10.1007/s00585-998-0721-6>
- Blanc, E., Mercandalli, B., & Houngninou, E. (1996). Kilometric irregularities in the *E* and *F* regions of the daytime equatorial ionosphere observed by a high resolution HF radar. *Geophysical Research Letters*, 23(6), 645–648. <https://doi.org/10.1029/96GL00415>
- Chisham, G., Lester, M., Milan, S. E., Freeman, M. P., Britow, W. A., Grocott, A., et al. (2007). A decade of the Super Dual Auroral Radar Network (SuperDARN): Scientific achievements, new techniques and future directions. *Surveys in Geophysics*, 28(1), 33–109. <https://doi.org/10.1007/s10712-007-9017-8>
- Chisham, G., Yeoman, T. K., & Sofko, G. J. (2008). Mapping ionospheric backscatter measured by the SuperDARN HF radars—Part 1: A new empirical virtual height model. *Annales Geophysicae*, 26, 823–841. <https://doi.org/10.5194/angeo-26-823-2008>
- Custovic, E., McDonald, A. J., Whittington, J., Elton, D., Kane, T. A., & Devlin, J. C. (2013). New antenna layout for a SuperDARN HF radar. *Radio Science*, 48, 722–728. <https://doi.org/10.1002/2013RS005156>
- Custovic, E., Nguyen, H., Devlin, J., Whittington, J., Elton, D., Console, A., et al. (2011). Evolution of the SuperDARN antenna: Twin terminated folded dipole antenna for HF systems. In *7th international conference on broadband communications and biomedical applications*, IEEE, pp. 24–29. <https://doi.org/10.1109/IB2Com.2011.6217936>

## Acknowledgments

C. M. M. is supported by TETFund (Ref. FUO/APRA/TETF.ASTD/14/15/002). M. K. J., S. E. M., and T. K. Y. were supported by STFC Grant ST/H002480/1. C. M. M. acknowledges valuable discussions with Dr. E. C. Thomas and M. J. Parsons on SuperDARN antenna system. The authors would like to thank the IRI and IGRF teams for providing the ionospheric and magnetic field models employed in the study. We acknowledge the role of the STFC/GCRF funded African Space Weather Workshop (Grant ST/R002932/1) hosted in Leicester in June 2018 in the formulation of this study. This research used the SPECTRE High Performance Computing Facility at the University of Leicester. The IGRF magnetic field model (<https://doi.org/10.1186/s40623-015-0228-9>) used in this study is freely available at <https://www.ngdc.noaa.gov/IAGA/vmod/igrf.html> (last accessed: 25 November 2019). The IRI Ionospheric models (<https://doi.org/10.1051/swsc/2014004>) used in this study are freely available at <http://irimodel.org/IRI-2012/> (last accessed: 25 November 2019).

- Davies, K. (1990). *Ionospheric radio*. London, U.K: The Institution of Engineering and Technology.
- de Larquier, S., Ponomarenko, P., Ribeiro, A. J., Ruohoniemi, J. M., Baker, J. B. H., Sterne, K. T., & Lester, M. (2013). On the spatial distribution of decameter-scale subauroral ionospheric irregularities observed by SuperDARN radars. *Journal of Geophysical Research: Space Physics*, 118, 5244–5254. <https://doi.org/10.1002/jgra.50475>
- de Larquier, S., Ruohoniemi, J. M., Baker, J. B. H., Varrier, N. R., & Lester, M. (2011). First observations of the midlatitude evening anomaly using Super Dual Auroral Radar Network (SuperDARN) radars. *Journal of Geophysical Research*, 116, A10321. <https://doi.org/10.1029/2011JA016787>
- Farges, T., Blanc, E., & Villain, J. P. (1999). Interpretation of equatorial electrojet irregularities observed with a broad beam H zenithal radar. *Radio Science*, 34(5), 1141–1152. <https://doi.org/10.1029/1999RS900049>
- Greenwald, R. A., Baker, K. B., Dudeney, J. R., Pinnock, M., Jones, T. B., Thomas, E. C., et al. (1995). DARN/SuperDARN: A global view of the dynamics of high-latitude convection. *Space Science Reviews*, 71(1), 761–796. <https://doi.org/10.1007/BF00751350>
- Greenwald, R. A., Frissell, N., & de Larquier, S. (2017). The importance of elevation angle measurements in HF radar investigations of the ionosphere. *Radio Science*, 52, 305–320. <https://doi.org/10.1002/2016RS006186>
- Hanuise, C., & Crochet, M. (1977). Multi-frequency HF radar studies of plasma instabilities in Africa. *Journal of Atmospheric and Solar-Terrestrial Physics*, 39(9), 1097–1101. [https://doi.org/10.1016/0021-9169\(77\)90018-6](https://doi.org/10.1016/0021-9169(77)90018-6)
- Hanuise, C., & Crochet, M. (1978). Oblique HF radar studies of plasma instabilities in the equatorial electrojet in Africa. *Journal of Atmospheric and Solar-Terrestrial Physics*, 40(1), 49–59. [https://doi.org/10.1016/0021-9169\(78\)90107-1](https://doi.org/10.1016/0021-9169(78)90107-1)
- Hanuise, C., & Crochet, M. (1979). Marginal plasma waves in the equatorial electrojet observed by HF coherent radar techniques. *Astrophysics and Space Science Library*, 74, 149–159.
- Hanuise, C., & Crochet, M. (1981a). 5–50-m wavelength plasma instabilities in the equatorial electrojet, 1. Cross-field conditions. *Journal of Geophysical Research*, 86(A5), 3561–3566. <https://doi.org/10.1029/JA086iA05p03561>
- Hanuise, C., & Crochet, M. (1981b). 5–50-m wavelength plasma instabilities in the equatorial electrojet 2. Two-stream conditions. *Journal of Geophysical Research*, 86(A5), 3567–3572. <https://doi.org/10.1029/JA086iA05p03567>
- Jones, R. M., & Stephenson, J. J. (1975). A versatile three-dimensional ray tracing program for radio waves in the ionosphere. Boulder, Colo: Office of Telecommun., U.S. Dep. of Commerce.
- Lawal, H. A., Lester, M., Cowley, S. W. H., Milan, S. E., Yeoman, T. K., Provan, G., et al. (2018). Understanding the global dynamics of the equatorial ionosphere in Africa for space weather capabilities: A science case for AfrequaMARN. *Journal of Atmospheric and Solar-Terrestrial Physics*, 192, 104765. <https://doi.org/10.1016/j.jastp.2018.01.008>
- Milan, S. E., & Lester, M. (2001). A classification of spectral populations observed in HF radar backscatter from the E region auroral electrojets. *Annales Geophysicae*, 19, 189–204. <https://doi.org/10.5194/angeo-19-189-2001>
- Milan, S., Yeoman, T., Lester, M., Thomas, E., & Jones, T. (1997). Initial backscatter occurrence statistics from the CUTLASS HF radars. *Annales Geophysicae*, 15(6), 703–718. <https://doi.org/10.1007/s00585-997-0703-0>
- Nishitani, N., & Ogawa, T. (2005). Model calculations of possible ionospheric backscatter echo area for a mid-latitude HF radar. *Advances in Polar Upper Atmosphere Research*, 19, 55–62.
- Nishitani, N., Ruohoniemi, J. M., Lester, M., Baker, J. B. H., Koustov, A. V., Shepherd, S. G., et al. (2019). Review of the accomplishments of mid-latitude Super Dual Auroral Radar Network (SuperDARN) HF radars. *Progress in Earth and Planetary Science*, 6:27, 1–57. <https://doi.org/10.1186/s40645-019-0270-5>
- Ribeiro, A., Ruohoniemi, J., Baker, J., Clausen, L., de Larquier, S., & Greenwald, R. (2011). A new approach for identifying ionospheric backscatter in midlatitude superDARN HF radar observations. *Radio Science*, 46, RS4011. <https://doi.org/10.1029/2011RS004676>
- Ribeiro, A., Ruohoniemi, J., Baker, J., Clausen, L., Greenwald, R., & Lester, M. (2012). A survey of plasma irregularities as seen by the midlatitude Blackstone SuperDARN radar. *Journal of Geophysical Research*, 117, A02311. <https://doi.org/10.1029/2011JA017207>
- Richmond, A. D. (1973). Equatorial electrojet—II. Use of the model to study the equatorial ionosphere. *Journal of Atmospheric and Solar-Terrestrial Physics*, 35(6), 1105–1118. [https://doi.org/10.1016/0021-9169\(73\)90008-1](https://doi.org/10.1016/0021-9169(73)90008-1)
- Tariku, Y. A. (2015). TEC prediction performance of the IRI-2012 model over Ethiopia during the rising phase of solar cycle 24 (2009–2011). *Earth, Planets and Space*, 67, 140. <https://doi.org/10.1186/s40623-015-0312-1>
- Thébault, E., Finlay, C. C., Beggan, C. D., Alken, P., Aubert, J., Barrois, O., et al. (2015). International Geomagnetic Reference Field: The 12th generation. *Earth, Planets and Space*, 67(1), 79. <https://doi.org/10.1186/s40623-015-0228-9>
- Villain, J. P., Greenwald, R. A., & Vickrey, J. F. (1984). HF ray tracing at high latitudes using measured meridional electron density distribution. *Radio Science*, 19(1), 359–374. <https://doi.org/10.1029/RS019i001p00359>
- Yeoman, T. K., Chisham, G., Baddeley, L. J., Dhillon, R. S., Karhunen, T. J. T., Robinson, T. R., et al. (2008). Mapping ionospheric backscatter measured by the SuperDARN HF radars—Part 2: Assessing SuperDARN virtual height models. *Annales Geophysicae*, 26, 843–852. <https://doi.org/10.5194/angeo-26-843-2008>
- Yeoman, T. K., Wright, D. M., Stocker, A. J., & Jones, T. B. (2001). An evaluation of range accuracy in the Super Dual Auroral Radar Network over-the-horizon HF radar systems. *Radio Science*, 26(4), 801–813. <https://doi.org/10.1029/2000RS002558>
- Yizengaw, E., Moldwin, M., Zesta, E., Biouele, C., Damtie, B., Mebrahtu, A., et al. (2014). The longitudinal variability of equatorial electrojet and vertical drift velocity in the African and American sectors. *Annals of Geophysics*, 57, 231–238. <https://doi.org/10.5194/angeo-57-231-2014>